Fabrication and Characterization of a Hybrid Heterojunction Composed of N–Type Silicon and PEDOT:PSS

Illan Kramer

Master of Engineering

Electrical and Computer Engineering

McGill University

Montreal,Quebec

2006-08-31

A thesis submitted to the Faculty of Graduate Studies and Research in partial fulfillment of the requirements for the degree of Master of Engineering

Your file Votre référence
ISBN: 978-0-494-32602-2
Our file Notre référence
ISBN: 978-0-494-32602-2

DEDICATION

To my sister, Naomi.

ACKNOWLEDGEMENTS

I would like to thank Dr. Ishiang Shih and Dr. Steven Xiao for their support and guidance throughout the course of my degree. I would also like to thank Dr. Cheng-Kuei Jen for being my supervisor and fulfilling all aspects that role demands with enthusiasm. The research also could not have been carried out without equipment provided by Dr. Clifford Champness or fabricated by Don, Jozsef or Scott in the mechanical workshop.

I would like to thank the other graduate students in the Electronic Devices & Materials group of the ECE department at McGill University for helping to make my research experience more enjoyable. Jon Kaufman is owed many thanks for his helping me with LaTeXin the preparation of this thesis.

This document could also not be completed without both financial and moral support from my family. Finally, I would like to thank the NSERC IPS program in conjunction with Organic Vision Inc. for financial support and providing a worthwhile experience mixing industry with research.

ABSTRACT

A hybrid organic/inorganic heterojunction has been fabricated using an n–type silicon wafer ($<111>$, $3 < \rho < 6\ \Omega \cdot cm$) and a p–type polymer, PEDOT:PSS ($\rho = 1\ \Omega \cdot cm$). Standard fabrication techniques such as vacuum deposition and spin coating are required for fabrication and have been employed. I–V characteristics have been measured under both dark and illuminated conditions for different thicknesses of PEDOT:PSS as defined by the spin rate at which the polymer has been spin coated. The data has been analyzed and figures of merit such as series resistance, short circuit current, open circuit voltage, fill factor and efficiency have been calculated. The efficiency ranges to values as high as 0.63%, while the fill factor has been observed to be as high as 57%, both of which are improvements on previously reported hybrid heterojunctions built on n–type silicon wafers.

ABRÉGÉ

Une hétérojonction hybride, organique/inorganique, a été fabriquée avec une plaque de silicium de type n (<111>, $3 < \rho < 6\ \Omega \cdot cm$) et un polymère de type p, PEDOT:PSS. Des techniques de fabrication standards telles que le dépôt sous vide et le dépôt à la tournette ont été utilisées. Les caractéristiques I–V ont été acquises dans le noir et dans les cas sous la lumière pour des différentes épaisseurs de PEDOT:PSS qui sont gouvernées par vitesse à laquelle le polymère est déposé. Les résultats ont été analysés et les facteurs de mérite tels que la résistance en série, l'intensité en court-circuit, la tension en circuit ouvert, le facteur de remplissage et l'efficacité ont été calculés. L'efficacité varie jusqu'à 0.63%, alors que des facteurs de remplissage jusqu'à 57% ont été observés. Ces derniers chiffres indiquent une amélioration sur ce qui a été rapporté précédemment sur des hétérojonctions fabriquées sur des plaques de silicium de type n.

TABLE OF CONTENTS

LIST OF TABLES

LIST OF FIGURES

CHAPTER 1
Introduction

The dream to build fully organic polymer solar cells has been around as long as electrically conductive and light absorptive polymers have been. The benefits are many: abundance of materials; cheapness of purification; ease of fabrication. Unfortunately, there are also plenty of drawbacks: material degradation over time; relatively poor electrical and optical properties; and perhaps most importantly, a lack of historical knowledge.

The field of organic electronics in general is quite immature compared with its inorganic cousin. Organic polymer photovoltaics are even younger. The lack of overall knowledge within the scientific community about polymer photovoltaics has resulted in a slow beginning to finding the silicon photovoltaic cell's replacement.

On the inorganic side, silicon, gallium arsenide and other well known substrates have been used to make solar cells for years. Both optical and electrical properties of Si and GaAs photovoltaics are very well known, specialists around the world exist in every facet of their fabrication, and they have long lifetimes. Their downside, however, is cost of fabrication. Fabs producing high quality silicon and gallium arsenide spend a lot of money to remove any impurities and fabricate the highest quality and highest uniformity wafers. Clean rooms are expensive to build and operate; whereas polymers can be synthesized in a standard chemical laboratory.

As a stepping stone to fully understanding the potential of fully organic polymer photovoltaic cells, some in the scientific community have built hybrid organic/inorganic p–n junctions. In some cases, the organic materials are small molecules, whereas in others, they are polymers. The inorganic layer is typically a silicon or gallium arsenide substrate, but sometimes other substrates are used, such as titanium oxide or copper indium selenide. These devices take advantage of the well known behaviour, properties and fabrication techniques of the inorganic substrates and pair them with new organic materials with advantageous light absorbing or electricity conducting properties.

One such structure, theorized, fabricated and characterized in this work involves an n–type silicon substrate with a p–type organic polymer, PEDOT:PSS. Contact materials are chosen to minimize contact resistance at the polymer–metal and silicon–metal interfaces, thus allowing a true characterization of the hybrid heterojunction, not any Schottky junctions that may inadvertently appear at the contacts.

The main objectives of this present work are to:

1 Outline the physical basis for creating such a structure.

2 Propose a method of fabrication for a silicon/PEDOT:PSS junction.

3 Characterize this device for photovoltaic applications.

Fabrication techniques used in the present work include spin-coating, baking, photolithography, evaporation and soldering. Experiments undertaken include I–V characterization, C–V characterization, spectrophotometry and scanning electron microscope measurements.

A brief outline of what the reader can expect to find in this document is now provided. Chapter 1, the introduction, describes the motivation to build and analyze the device proposed in this document. Chapter 2 itemizes existing research done in this field, complete with fabrication techniques, performance measures and limitations of related devices. Chapter 3 introduces the physical basis and device theory necessary to design and optimize not only photovoltaic devices, but particularly hybrid organic/inorganic junctions. Chapter 4 simply describes the steps necessary to fabricate the proposed structure, as well as the measurement techniques employed. Chapter 5 provides the results of the measurements described in chapter 4 and analyzes them using the theoretical concepts discussed in chapter 3. Chapter 6 describes additional work that has been undertaken on this project that is not directly related to the main thrust of this present work, but that can be applicable to any future work on the topic. Chapter 7 lists the conclusions that can be derived from the results of this document as well as proposes any future work that can be carried out in order to further the understanding of this particular device, or any devices closely related to it.

While photovoltaic devices involving the use of n–type silicon or PEDOT:PSS have previously been fabricated and characterized, a structure consisting of both as the two layers forming the active region for a photovoltaic cell has not. This work, therefore, while having been inspired by previous hybrid devices, is new.

CHAPTER 2
Literature Review

This chapter provides a brief survey of the research work reported in the area of organic photovoltaics with particular attention given to hybrid organic/inorganic junctions. Particularly pertinent are devices where the inorganic material is silicon and is used as the n-type region in the p-n heterojunction.

The exact structure proposed in this thesis has previously been constructed by Smith and Forrest [1]. This device, however, was not fabricated for photovoltaic applications, but rather as a memory element where the organic material is used as an organic fuse. The energy band diagram shown in figure 3–7 is largely derived from the data outlined in this article.

Schubert et al. [2] have also created a structure similar to the one discussed in this thesis. The motivation, however, was not to determine photovoltaic properties of such a cell, but rather to identify certain electrical and physical properties.

The PEDOT:PSS was spin coated onto both p-type silicon wafers ($N_A \sim 5 \times 10^{18}$) and degenerately doped n-type silicon wafers ($N_D \sim 4 \times 10^{19}$). Both wafers had (100) crystallographic orientation. The spin rate employed was 3000 RPM followed by curing at $120°C$ for 5 min. Infrared spectroscopic ellipsometry (IRSE) was used to characterize the structure.

Using the IRSE, it was found that the structure on the p-type silicon yielded a depletion layer thickness of 35 nm; however, because the n-type silicon was degenerately doped, the depletion layer thickness was too small to detect using the IRSE.

Ltaief et al [3] have demonstrated a purely organic solar cell where the active region is known as a bulk heterojunction. The bulk heterojunction consists of MEH-PPV, a p-type polymer, blended with C_{60}, an n-type soccer ball shaped small molecule (also known as buckminsterfullerene or simply fullerene). The relative weight ratios of MEH-PPV and C_{60} were varied in order to optimize both photovoltaic and electroluminescent performance. The complete final device had the structure Glass/ITO/MEH-PPV+C_{60}/Al. The bulk heterojunction was fabricated by spin-coating the polymer/fullerene mixture at 2000 RPM for 20 s for a thickness of approximately 500 nm and an area of 10 mm^2. The aluminum cathode was deposited by thermal evaporation under high vacuum conditions (10^{-5} $Torr$).

The weight percentages of C_{60}/MEH-PPV+C_{60} tested were 1%, 3%, 6%, 9%, 10%, 20%, 30%, 40%. The absorption spectra of several of these blends show that the variation in C_{60} concentration affects the absorption only at short wavelengths, < 300 nm. A plot showing photoluminescent quenching vs. C_{60} concentration provides an indication of what the optimal photovoltaic blend is for light absorption. This does not, however, indicate that this will necessarily produce the most electrical power; merely that it formed excitons have a the lowest chance of radiatively recombining. Charge transport could still limit current flow at this ratio.

The most useful curve shown in this article is the J–V curve (where J represents current density) under illumination by white light of a halogen lamp (power delivered unspecified) indicating that the maximum J_{SC}, maximum V_{OC} and best fill factor are found at a blend of 3%. Table 2–1 summarizes the figures of merit tested in this article.

Finally, also discussed are the effects of the solvent into which the MEH-PPV is dissolved. The solvent can fairly drastically degrade or enhance the photovoltaic performance of the device by altering its absorption and emissions spectra.

Lotaief et al. [4] also studied a photovoltaic cell structure involving an intermediate PEDOT:PSS layer between the MEH-PPV/C_{60} bulk heterojunction and the ITO anode. The final result is the following structure: Glass/ITO/PEDOT:PSS/MEH-PPV+C_{60}/Al. The PEDOT:PSS is applied by spin-coating at 2000 RPM for 20 s followed by a short anneal at 120°C for 5 min. The bulk heterojunction is applied by spin coating and the aluminum cathode is evaporated using the same parameters as in [3].

This paper does a similar analysis to [3] only with varying the volume percentage of C_{60} in MEH-PPV. Photoluminescence is minimized at a 7 vol. % C_{60} concentration, meaning that charge separation is optimized at this blend of C_{60} and MEH-PPV. At such a low percentage, howevever, charge transport is rather poor as the conductivity is close to zero. Increasing this percentage to over 40 vol. % makes the mixture highly conductive but promotes radiative recombination, thus reducing its charge separation properties.

Shin et al. [5] have created a structure using polythiophene (PP-Th) as the organic polymer layer and n-type silicon. The PP-Th was polymerized using a plasma polymerization method consisting of a capacitively-coupled bell jar reactor operating under conditions of 13.56 MHz, 2.5 W and 75 $mTorr$ with Argon as the carrier gas and a thiophene partial pressure of 10 $mTorr$. The final device structure is Au/PP-Th/n-Si with a polymer layer thickness of 0.1 μm.

The device is illuminated using a xenon arc lamp at 82 mW/cm^2. The device is based under illumination at -3 V and is found to produce a photocurrent of 0.1 mA/cm^2. The photocurrent, however, drops off to nearly 0 mA/cm^2 at 0 V. This indicates that the cell is not, in its current state, useful for photovoltaic applications. An abundance of recombination centres or traps likely exist in the vicinity of the heterojunction preventing current flow at low voltages.

Since V_{OC} and J_{SC} both have values near the origin of the J-V curve, no meaningful data can be extracted with respect to the maximum power point, fill factor and efficiency of the cell. This device shows that while the PP-Th aids in absorption, it impedes the ability for current to arrive at the contacts under a small bias. These results are also summarized in table 2–1.

Camaioni et al. [6] [7] have created a structure where poly(4,4'-dipentoxy-2,2'-bithiophene) (poly(ET2)) is sandwiched between n-type silicon and aluminum. The polymer was deposited on the silicon using a cyclic voltammetry method. The silicon wafer acts as an anode and is illuminated with a tungsten lamp while being immersed in an electrolyte (tetrabuthylammonium) with the conductive polymer. The polymer layer is approximately 2 μm. The aluminum contacts on both the silicon backside

and on the polymer were deposited using vacuum evaporation through a shadow mask to form a device area of 0.5 cm^2.

J-V measurements are done using a xenon arc lamp employing a filter to remove unwanted IR radiation. The lamp was operated at three different light intensities, however, for brevity, only the most intense (6.8 mW/cm^2) is listed in table 2–1.

Yuan et al. [8] have created both p-n and p-p junctions using polyaniline (PAn) and silicon. The PAn films were polymerized and deposited simultaneously using an electrochemical polymerization technique for the p-type silicon wafer and by a photoelectrochemical polymerization technique for the n-type silicon wafer (i.e. the same technique as with the p-type wafer, only under illumination). The type of metal and method of metal deposition for metal contacts was not specified.

While both the p-p and p-n heterojunctions demonstrated current rectification (rectification ratio of 50 for p-n heterojunction), only the p-n junction showed a significant photocurrent. The device area was not listed and thus the current density in table 2–1 is shown over "A", where A is the device area.

Using a C-V measurement, it can be determined that the carrier concentration in the PAn is 1.1×10^{17} cm^{-3}. It can also be determined that for n-type silicon of carrier concentration 4.6×10^{15} cm^{-3}, the depletion depth is 0.38 μm on the n-type silicon side and 0.02 μm on the PAn side. The junction barrier is 0.51 V in the conduction band and only 0.05 V in the valence band.

Laranjeira et al. [9] have fabricated a device very similar to [8]. The polyaniline (PAn) was deposited using a spin coating technique onto a silicon wafer (n-type, (100) crystallographic orientation, 1 Ωcm) to form a 40 nm thick layer. Electrical

contacts of gold were vacuum evaporated through a shadow mask to form a device area of 0.0036 cm^2 on the PAn. The backside contact of aluminum was also vacuum evaporated.

The device rectifies current to a much higher degree than in [8] by 3 orders of magnitude in the rectification ratio. The device was not measured under illuminated conditions, but conclusions regarding the series resistance were reported and can be found in table 2–1.

Musa and Eccleston [10] have fabricated a device consisting of a regioregular poly(3-octylthiophene) (P3OT) on both n-type (n-Si) and p-type (p-Si) silicon with crystallographic orientation of (100). The P3OT was deposited by spin coating, forming a polymer layer thickness of 200–300 nm. Both gold and aluminum metal contacts were deposited on the P3OT through a shadow mask to form the device area (0.00314 cm^2).

The rectification ratio of this device is on the order of 10^6 for the Al/P3OT/p-Si structure. Of the three structures tested (namely: Al/P3OT/p-Si, Au/P3OT/p-Si and Al/P3OT/n-Si), this one had the highest rectification ratio. The Al/P3OT/p-Si device is also characterized under white light illumination (incident power unspecified). The reverse current increases by three orders of magnitude when illuminated (from nanoamperes to microamperes). The results can be found in table 2–1.

Yang et al [11] have fabricated devices using polypyrrole (PPy) on n-type (111) silicon (n-Si) and using polyaniline (PAn) on n-type (111) silicon. The polymer was electrodeposited onto the silicon substrate. The entire cell structure was as follows: ITO/PPy or PAn/n-Si/ITO.

A surface photovoltage spectroscopy (SPS) method was used to determine the spectroscopic response of the cells. It was found that the PAn/n-Si cell produced nearly an order of magnitude increase in photovoltage throughout the visible light range compared with the PPy/n-Si cell or a simple n-Si cell with no polymer. Furthermore, it was shown that when biased at $-3\ V$, the PAn/n-Si cell showed further photovoltage improvement (once again by a factor of 10) throughout the visible light range.

Using the SEM, it was observed that the PPy film was of relatively poor quality compared with the PAn film. This could have lead to the degradation of spectroscopic response as measured by the SPS. A surface electric field is proposed as the reason for the increase in photovoltage due to reverse bias.

Devices involving inorganic materials other than silicon or gallium arsenide forming a heterojunction with organic polymers have also been realized. Song et al. [12] have fabricated two device structures. The two structures are ITO/TiO_2/MEH-PPV/Au and ITO/TiO_2/MEH-PPV/PEDOT/Au.

The devices were fabricated by spin coating TiO_2 onto the ITO covered glass substrate at 3000 RPM followed by an anneal for 30 min at $450°C$ in air to form a thickness of 700 nm. The MEH-PPV was spin coated as well in order to create a 100 nm thick layer. PEDOT was then also spin coated at 1000 RPM. The gold contact was vacuum evaporated. The device active area was 0.18 cm^2 and were illuminated by a 50 mW/cm^2 xenon arc lamp to produce the J–V curves. The results are listed in table 2–1.

The improved performance of the device containing the PEDOT layer is due to the reduced series resistance evident on the J–V curve. While the values are not listed specifically, it can be seen that the current allowed to flow at high forward bias is much higher in the PEDOT device than in the other device.

Arango et al. [13] have also created a structure with the inorganic material being a titanium oxide and compared it to a purely organic junction. Both devices contain a layer of phenylamino-p-phenylenevinylene (PA-PPV) that forms the primary organic layer. The two structures explored are ITO/TiO_X/Pa-PPV/Au and ITO/PEDOT/PA-PPV/Al.

The PA-PPV layer is 80 *nm* thick in the TiO_X device and is 100 *nm* thick in the PEDOT device. The open circuit voltages are listed for the two devices and the fill factor is listed as well for the TiO_X device. Several different thicknesses of PA-PPV on TiO_X are also tested and show that decreasing the thickness from 300 *nm* to 80 *nm* more than doubles the fill factor. Quantum efficiency is also shown, but only as a function of input wavelength, not in response to a white light source and thus is not listed along with the rest of the data in table 2–1.

Bereznev et al. [14] have fabricated three photovoltaic structures using $CuInSe_2$ (CIS) as the inorganic material for the heterojunction and either PPy or PEDOT-PSS as the organic polymer. The material for the front contact window was either gold or a combination of intrinsic zinc oxide (i-ZnO) and n-doped zinc oxide (n-ZnO). The back contact in each case was copper. The topography of the three structures are as follows: Cu/CIS/PPy/i-ZnO/n-ZnO, Cu/CIS/PEDOT-PSS/Au and Cu/CIS/PEDOT-PSS/i-ZnO/n-ZnO.

Polycrystalline CIS was purchased already on a copper substrate. PPy was electrophotochemically polymerized onto the CIS surface under white light illumination at 100 mW/cm^2 while PEDOT was spin coated then dried for 24 h at 40°C. The PPy thickness was measured to approximately 500 nm while the PEDOT-PSS thickness was measured to be 50 nm. The ZnO layers were RF sputtered. The i-ZnO layer was 100 nm with the n-ZnO layer being 900 nm. For the gold device, vacuum evaporation was used for deposition.

The device was illuminated at 100 mW/cm^2 to determine its photovoltaic J–V characteristics. The results are found in table 2–1 with PEDOT-PSS listed simply as PEDOT for brevity.

Garnier [15] has fabricated a hybrid organic-on-inorganic structure where the inorganic material is n-type gallium arsenide (n-GaAs) and the organic material is poly(3-methylthiophene), PMeT, a p-type polymer. The n-GaAs wafer used is (100)-oriented and has a doping level of 2×10^{16} cm^{-3}.

The back contact was formed by evaporating an alloy of Au and Ge followed by a 400°C anneal in an N_2 environment. Unlike in previous papers discussed, the polymer was not spin-coated, but instead a method of electropolymerization was employed. The polymer is grown under tungsten lamp illumination to thicknesses ranging from 6 to 100 nm. The top contact was then formed by evaporating a layer of Au to a thickness of approximately 15 nm. It was found that this thickness of gold only allowed 20 % of the incident light to pass through. The active area of the device is 0.25 cm^2.

The cell was tested and compared to a Schottky cell whose structure is the same as the above cell except without a polymer layer between the n-GaAs and Au contact. All testing was performed under an Oriel xenon arc lamp. The results are summarized in table 2–1.

Yang et al. [16] have created purely organic bulk heterojunctions using MEH-PPV mixed with C_{60}. In order to improve device performance, they have attempted to dope this bulk heterojunction with various other small-molecule organic materials. The dopants (and their percentages within the MEH-PPV + C_{60} mixture by weight) that have been used are: poly(N,N'-diphenyl-4-styrene), p-TPA (50%); Tetrachloroquinone, TCQ (0.5%); 2-(biphenyl-4-yl)-5-(4-tert-butylphenyl)-(1,3,4-oxadiazole), PBD (20% and 40%); N,N'-diphenyl-(1,1'-biphenyl)4,4'-diamine, TPD (20% and 40%); and triphenylamine, TPA (20% and 40%). The final device structure was ITO/PEDOT:PSS/MEH-PPV+C_{60}+dopant/Al.

PEDOT:PSS is spin coated over ITO covered glass. The MEH-PPV+C_{60}+dopant layer is then also spin coated. The top contact is formed using vacuum evaporation of aluminum. The active device area is 0.12 cm^2.

The J–V measurements are carried out using a xenon arc lamp. The performance improvement is maximized when the dopant is TPA in a concentration of 40%, and thus only this configuration is listed in table 2–1 with the MEH-PPV+C_{60} bulk heterojunction listed simply as BHJ.

Tokranova et al. [17] have created a device that takes utilizes the modified energy band diagram of nano-porous silicon (PSi). The PSi was used to to absorb light of different wavelengths than monocrystalline silicon. A small-molecule organic

material, in this case copper phthalocyanine (CuPC) was used to fill the nanoporous structure and create the desired band bending for effective charge separation.

Fabrication began with an n-type silicon wafer with resistivity 0.025 Ωcm and crystallographic orientation (100). The PSi film was fabricated by using an electrochemical etching process of silicon in a solution of hydrofluoric acid diluted in ethanol. The PSi was filled by dropping a solution of CuPC onto the surface and mechanically applying pressure for 30 s to form a layer thickness of 15 nm. The front side contacts were formed by sputtering of gold or ITO onto the CuPC through a shadow mask while the backside contacts were fabricated by vacuum evaporation of aluminum or chromium and gold. The active area of the cell was 0.05 cm^2.

The devices were tested under a tungsten lamp operating at 33 mW/cm^2. Two different thicknesses of PSi were tested: 1.8 μm and 12 μm. The results are described in table 2–1.

Kushto et al. [18] have fabricated two devices using two small-molecule organic materials to form a p-n junction. N,N'-(α-naphthyl)-N,N'-diphenyl-1,1'-biphenyl-4,4'-diamine (α-NPD) formed one layer while C_{60} formed the other. One device structure used ITO covered glass, while the other used PEDOT:PSS coated on polyethersulphone (PES), a flexible substrate. Both devices used a combination of magnesium and silver to form the contact over the C_{60} layer.

For the PES/PEDOT:PSS/α-NPD/C_{60}/Mg:Ag device, the PEDOT:PSS was spin coated onto the PES (PEDOT:PSS thickness of 85 nm) and cured at 150°C. The organic materials were sublimated directly onto the surface of the device (α-NPD and C_{60} thicknesses of 10 nm and 48 nm, respectively) followed by vacuum

evaporation of magnesium and gold. For the ITO/PEDOT:PSS/α-NPD/C_{60}/Mg:Ag, a low conductivity PEDOT:PSS was spin coated onto the ITO covered glass (low conductivity PEDOT:PSS thickness of 30 nm). The organic materials and metal contacts were deposited in the same way and at the same thickness as the other device. The device area was 0.04 cm^2.

The devices were illuminated using a xenon arc lamp operated at three light intensities: 11 mW/cm^2, 97 mW/cm^2, and 208 mW/cm^2. Table 2–1 only outlines the results for the 97 mW/cm^2 light intensity for brevity.

Table 2–1 below summarizes the figures of merit either specifically specified or interpolated from figures in the articles discussed previously. Many of the figures of merit were not listed, nor could be derived from the figures and are thus not summarized in the table.

Table 2–1: Figures of merit reported in literature review articles.

Sample	R_S $(\Omega \cdot cm^2)$	J_{SC} $(\frac{mA}{cm^2})$	V_{OC} (V)	MPP (μW)	FF (%)	η (%)
[3] ITO/MEH–PPV+C_{60}/Al	–	55×10^{-6}	1.38	0.0048	63	–
[5] n-Si/PP-Th/Au	–	~0	~0	–	–	–
[6] n-Si/poly(ET2)/Al	~100	0.22	0.34	–	40	0.43
[8] n-Si/PAn	–	0.095/A	0.2	–	–	–
[9] n-Si/PAn/Au	14.4	–	–	–	–	–
[10] p-Si/P3OT/Al	–	0.029	0.3	–	–	–
[12] TiO_2/MEH-PPV/Au	–	0.55	0.79	24	31	0.28
[12] TiO_2/MEH-PPV/PEDOT/Au	–	0.57	0.70	46	64	0.51
[13] TiO_X/PA-PPV/Au	–	–	0.85	–	52	–
[13] PEDOT/PA-PPV/Al	–	–	0.7	–	–	–
[14] CIS/PPy/i-ZnO/n-ZnO	–	5.7	0.5	–	–	–
[14] CIS/PEDOT/Au	–	20	0.5	–	–	–
[14] CIS/PEDOT/i-ZnO/n-ZnO	–	5.7	0.4	–	–	–
[15] n-GaAs/Au	–	10	0.42	703	67	14
[15] n-GaAs/PMeT/Au	–	8.4	0.7	940	64	17.5
[16] PEDOT/BHJ+TPA/Al	–	0.79	0.66	25	40	0.24
[17] n-Si/PSi(1.8 μm)+CuPC/ITO	–	7.4	0.24	26	29	1.6
[17] n-Si/PSi(12 μm)+CuPC/ITO	–	7.56	0.33	50	40	3
[18] PES/PEDOT/α-NPD/C_{60}/Mg	118	~3	0.85	–	–	1
[18] ITO/PEDOT/α-NPD/C_{60}/Mg	40	~2.5	0.85	–	–	1

CHAPTER 3
Theory on Organic/Inorganic Hybrid Photovoltaics

The physical basis of photovoltaic devices and in particular organic photovoltaics is outlined in several textbooks, such as [19] and [20], the main points of which are described in this chapter. The design of photovoltaic devices consists primarily of selecting appropriate materials and arranging them in a structure conducive to the conversion of light into electricity. This chapter outlines in detail what considerations are important in these two aspects of photovoltaic device design: notably light absorption, charge separation and charge transport. In addition, several figures of merit will be discussed in order to quantify the performance characteristics of the devices in question.

3.1 Light Absorption

The most important element of any photovoltaic device is the layer that absorbs light. For any material the bandgap (the region between the valence and conduction bands for inorganic materials or the region between the HOMO (highest occupied molecular orbital) and LUMO (lowest unoccupied molecular orbital) for organic materials) determines the wavelength at which absorption can begin. The relationship between the wavelength of the minimum energy incident photon to be absorbed and the material bandgap is shown in equation 3.1.

$$\nu_{photon} = \frac{E_G}{h} = \frac{c}{\lambda_{photon}} \tag{3.1}$$

In equation 3.1, ν_{photon} and λ_{photon} are the frequency and wavelength, respectively, of the incident photon, E_G is the bandgap of the light absorbing material, h is Planck's constant, and c is the speed of light in a vacuum. Clearly, it can be seen that the bandgap energy is inversely proportional to the wavelength of light absorbed.

Light absorption consists of a photon of a given energy bombarding a material creating an electron hole pair also known as an exciton. The relative positions of the electron hole pair on the energy band diagram is equal to the energy of the incident photon. The density of holes and electrons at different energy levels within the conduction and valence bands dictates the ability of a certain wavelength of light to be converted into electricity within the light absorbing medium. Figure 3–1 shows a stylized example of an incident photon promoting an electron in the valence band to the conduction band and leaving a mobile hole behind in the valence band. This example describes light absorption for inorganic materials, although the process is analogous for organic materials.

Because the distribution of carriers varies with energy, it is natural that the ability of a material to absorb light will vary with the wavelength of that light. This variation in absorption with respect to wavelength is called the absorption spectrum of a material.

The absorption coefficient, α, describes how well light gets absorbed as it passes through a material of a given thickness. α is typically described in units of cm^{-1},

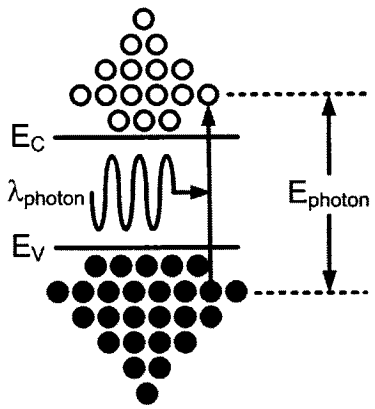

Figure 3–1: Energy band diagram depicting light absorption.

although it is sometimes described with unitless dimensions as a relative intensity. A low absorption coefficient results in low absorption of light per *cm*. For thin absorption layers in a device, a high absorption coefficient is thus desired so that very little light passes through unabsorbed. A low absorption coefficient can, however, be tolerated for relatively thick devices. In general, the larger the bandgap, the smaller the value of the absorption coefficient at a given energy, although the densities of states in the conduction and valence bands as well as the directness or indirectness of the bandgap are also factors.

Direct bandgap materials are materials in which the conduction band minimum and valence band maximum align at the same value of momentum, k. If this criterion is not met, then the material is said to be indirect, and transitions from conduction to valence band (or vice versa) require an additional process in order to overcome the momentum difference. This difference is shown in figure 3–2 with the sideways arrow in the indirect case representing a phonon-assisted transition.

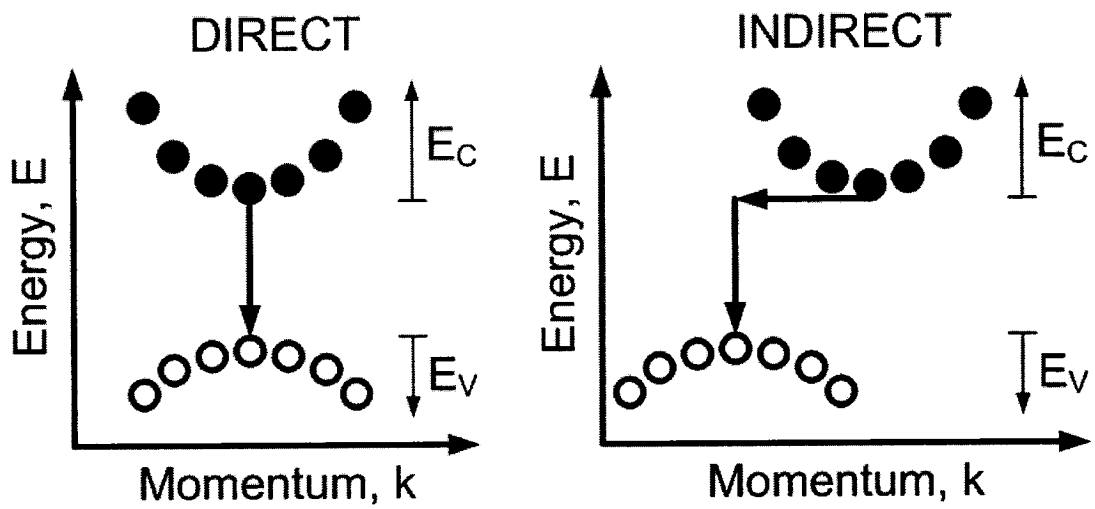

Figure 3–2: $E - k$ diagram for direct and indirect semiconductors.

The device proposed in this thesis consists of a 0.5 *mm* thick n-type silicon wafer as well as a thin PEDOT:PSS layer. The absorption spectra of these two materials can be seen in the Experimental Results chapter.

3.2 Charge Separation

Light absorption is not the sole consideration when selecting appropriate materials for photovoltaic cells. As was seen in the previous section, the bombardment of a photon on a material generates an exciton. If no field exists in the immediate vicinity of the exciton, then it will likely be destroyed by the recombination of the free hole and free electron. The recombination may be radiative or non-radiative, but in either case, the light absorption is wasted as the charge does not reach the contacts. Charge separation is essential to utilizing the absorbed light and transferring it to the outside world.

Charge separation is the process of physically moving the electron away from the hole in order to prevent recombination. This is most commonly done by the presence of a strong electric field. The depletion region of a PN-junction is sufficient to create this charge separation, thus steering the electrons to one contact while steering the holes to the other contact. Figure 3–3 shows how the presence of an internal electric field caused by a PN-junction can steer charges in opposite directions from each other. Electrons drift toward the lower energy state while holes drift toward the higher energy state as is consistent with the drift current principle in a PN-junction.

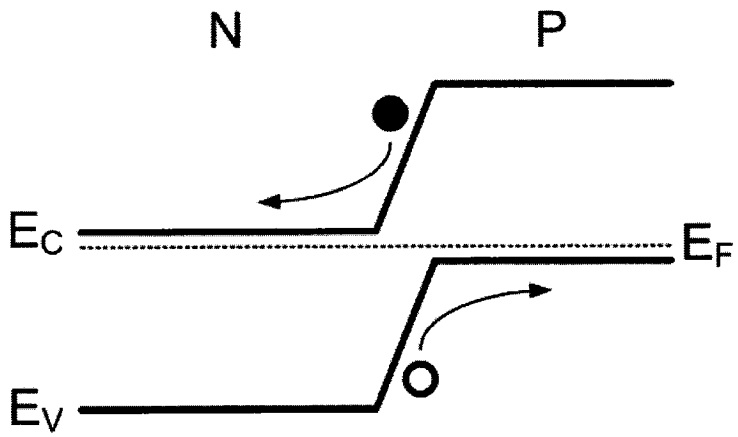

Figure 3–3: Energy band diagram showing the charge separation of a photogenerated electron hole pair.

It should be noted that the electric field creating charge separation does not need to be realized through a PN-junction. A Schottky junction is also capable of causing electron and/or hole drift. A Schottky junction uses a single light absorbing layer. The electric field necessary for charge separation arises from the difference between the work function of one (or both) of the metal contacts and the light

absorbing semiconductor. Figure 3–4 shows how an electric field can be created in a metal/semiconductor junction. From this energy band diagram, it can be seen how photogenerated holes would drift toward the gold contact while photogenerated electrons would drift away from it.

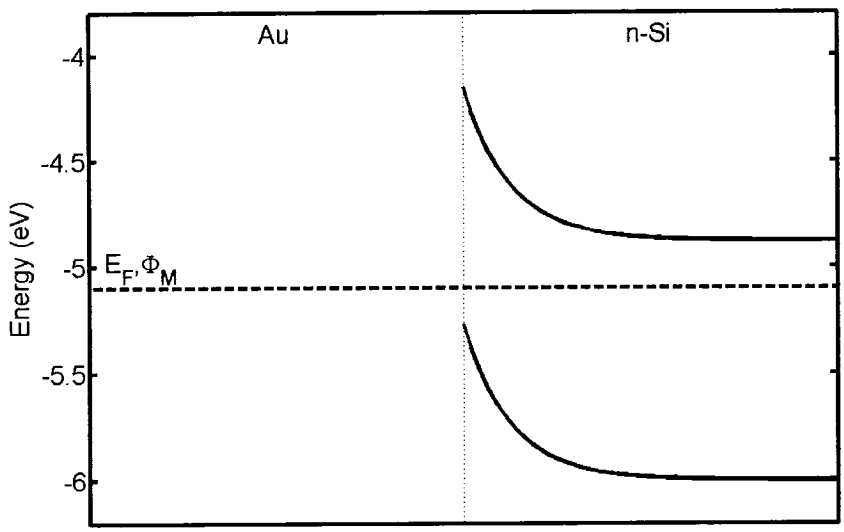

Figure 3–4: Energy band diagram of a Schottky junction.

The performance of the gold/n-type silicon Schottky junction shown in figure 3–4 is used as a standard by which to compare the results of the structure proposed in this thesis.

3.3 Charge Transport

Of course, once the junction is created and the charges can be separated, it becomes critical to ensure that the photogenerated charges can actually arrive at the edge of the depletion region. This is primarily governed by the minority carrier

lifetime of free holes in an n-type material, τ_p, and free electrons in a p-type material, τ_n.

The simplest case scenario of photogeneration and charge separation can be seen in figure 3–3, but rarely do the majority of excitons become generated within the depletion region. This is primarily due to the thinness of the depletion region relative to the large thickness of the bulk regions. In the case where the majority of light is absorbed in the bulk region of the PN-junction, it becomes necessary to ensure that the minority photogenerated carrier will have a lifetime long enough to arrive at the edge of the depletion region and be swept through it. A long minority carrier lifetime is thus highly desirable for the material in which the majority of light absorption takes place.

Once again, the directness or indirectness of the material becomes a critical factor. Because of the additional requirement of a photogenerated carrier to interact with a phonon prior to decaying to the valence (for an electron) or conduction (for a hole) band, the minority carrier lifetime in an indirect bandgap semiconductor is much higher than that of a direct bandgap semiconductor. Essentially, a minority carrier has to "wait" for a phonon of appropriate momentum to interact with it before it can recombine.

3.4 Conductive Polymers

The movement of charged particles in an inorganic solids has been researched and well understood for decades. It involves a weakly bonded electron receiving enough energy to break free from the atom to which it is bonded and move freely through the crystalline lattice.

Alternatively, the movement of charged particles in conductive polymers depends on the type of bond between atoms along the carbon backbone of the long molecule. While σ-bonds involve tightly bound electrons that are incapable of movement, π-bonds involve relatively loosely bound electrons that are free to move along the chain of carbon atoms making up the polymer.

An illustration of how current flows down the carbon backbone of a conjugated polymer, in this case polyacetylene, is shown in figure 3–5.

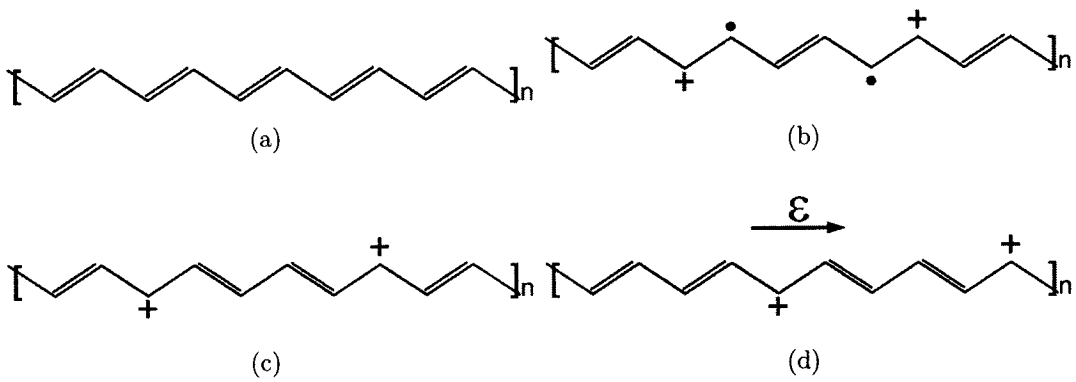

Figure 3–5: Current flow through polyacetylene, a conjugated polymer

Figure 3–5(a) shows the initial structure of polyacetylene showing alternating double and single bonds. An element with high electron affinity is added in figure 3–5(b) in order to remove some electrons from the polyacetylene chain. Figure 3–5(c) shows that the electrons reorganize themselves so that no dangling bonds are left in the chain. If an electric field is applied, the positive charges are free to move down the polymer resulting in a net current flow as shown in figure 3–5(d).

The example just shown helps to explain electron motion within the molecule; however, molecule-to-molecule motion is limited by an electron "jumping" from one

molecule to the next. The ability to arrange molecules in a predefined order thus can have a profound impact on conductivity. Some common polymers used for organic photovoltaic applications can be seen in figure 3–6.

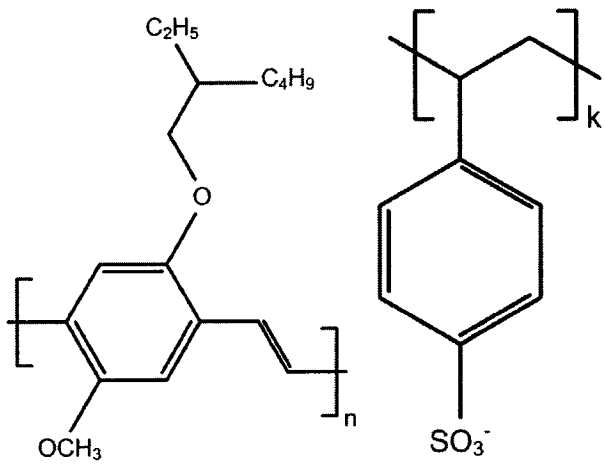

(a) MEH-PPV [21] (b) PSS [22]

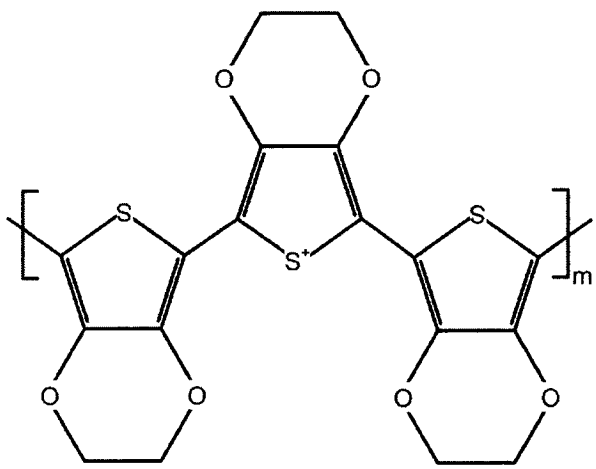

(c) PEDOT [22]

Figure 3–6: Some polymers that are commonly used in organic photovoltaics.

MEH-PPV, poly[2-methoxy-5-(2'-ethyl-hexyloxy)-1,4-phenylene vinylene], is often used in OLEDs, but has also been researched for organic photovoltaic applications. PEDOT, poly(3,4-ethylenedioxythiophene), and PSS, poly(styrenesulfonate), are typically mixed together to form a macromolecular salt; this mixture is commonly referred to as PEDOT:PSS and comes in two types: a conductive grade (Aldrich 483095) 1.3 *wt.* % dispersion in H_2O (0.5 *wt.* % PEDOT content, 0.8 *wt.* % PSS content), and a low conductivity grade (Aldrich 560596) 2.8 *wt.* % dispersion in H_2O (0.14 *wt.* % PEDOT content, 2.6 *wt.* % PSS content). PEDOT:PSS is often used in OLEDs as well, but is also a promising for the field of organic photovoltaics.

3.5 Materials Selection

The inorganic material was chosen to be n-type silicon as it is widely available, is well documented from both a processing and material properties perspective, and is relatively cheap when compared to other monocrystalline inorganic light absorbing materials.

The structure of the device proposed and characterized in this thesis morphed over the course of the study. Initially, the intention was to create a hybrid heterojunction between n-type silicon and p-type MEH-PPV, a conductive polymer. It was hoped that the MEH-PPV would be capable of absorbing wavelengths of light that the silicon would not be capable of absorbing and thus photocurrent would be enhanced compared to a simple gold/n-type silicon Schottky junction. It was found, however, that the photocurrent was several orders of magnitude lower than that of the Schottky junction.

A structure using a more conductive polymer, such as conductive grade PEDOT:PSS, was used in place of the MEH-PPV due to the realization that the organic material was contributing very little to the light absorption, but its role was more significantly to enhance charge separation and provide good charge transport. The more highly conductive PEDOT:PSS was thus selected as the organic material to be used for the hybrid heterojunction. The results from the MEH-PPV/n-type silicon junction are omitted from this document for brevity; however, the results from the PEDOT:PSS/n-type silicon junction can be found in the Experimental Results section.

3.6 Energy Band Diagram

The energy band diagram shown in figure 3–7 (modified from [1]) is stretched in the x-axis to illustrate the variations in energy at the junctions between materials. Experiments conducted on the device involved different thicknesses of PEDOT:PSS that are not illustrated in the figure. In addition, the thickness of the n-type silicon is orders of magnitude thicker than the PEDOT:PSS; however, this is also not illustrated in the figure.

Figure 3–7 does indicate that the junction between the PEDOT:PSS and gold contact window, while not ohmic, is very close to ohmic and thus does not pose an imposing barrier for free charges as in a Schottky junction. In addition, the barrier formed between the PEDOT:PSS and n-type silicon is shown, indicating the electric field present to separate excitons and steer free charges.

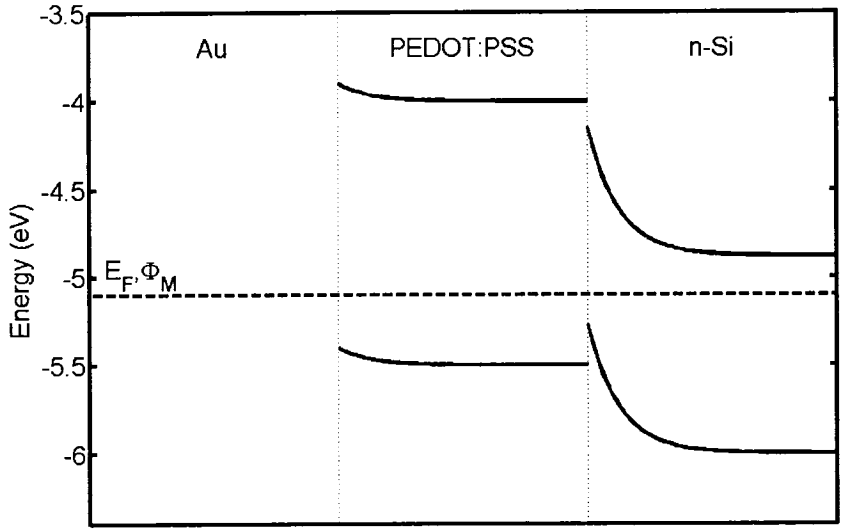

Figure 3–7: Energy band diagram of hybrid photocell.

Omitted from figure 3–7 is the junction between the n-type silicon and the Wood's metal contact. This has been shown in the past to be ohmic, resulting in no further electric field to impede or enhance the motion of free charges.

3.7 Final Device Geometry

The final device structure fabricated for analysis is shown in figure 3–8. A detailed description of the fabrication procedures is outlined in the Experimental Procedure chapter.

The features of note in figure 3–8 are the non-conductive polyimide passivation layer containing openings forming the junction area, the thin layer of PEDOT:PSS applied by a spinner and cured in an oven, the thin and thick gold contacts formed

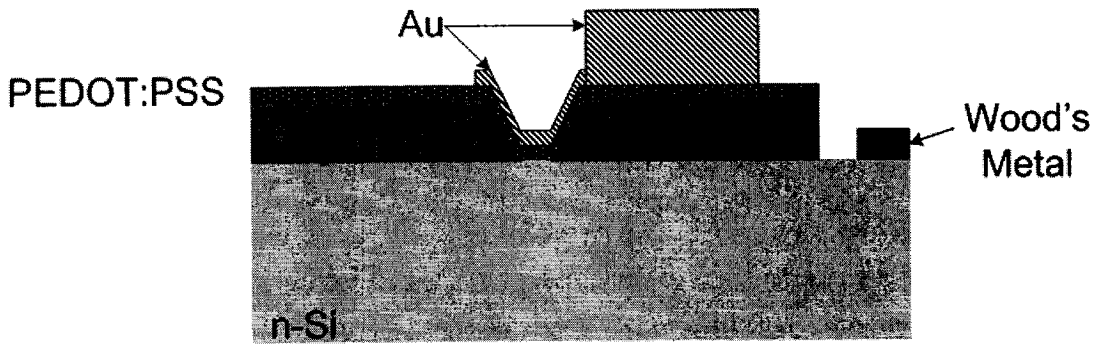

Figure 3–8: Device cross-section of hybrid photocell

by evaporation in conjunction with a metal shadow mask and the negative Wood's metal contact applied using a simple soldering iron.

Some light is reflected and/or absorbed by the thin gold contact, but the light that passes through becomes absorbed by either the thin PEDOT:PSS layer or by the thick n-type silicon layer. The depletion region separates the charges and directs them either to the Wood's metal contact (free electrons) or toward the gold contact (free holes).

3.8 Organic Photovoltaic Figures of Merit

Traditional figures of merit for photovoltaics are, of course, also applicable to photovoltaic devices employing organic materials. These include, primarily: short circuit current (I_{SC}), open circuit voltage (V_{OC}), fill factor (FF), series resistance (R_S) and maximum power delivered (MPP).

The short circuit current and open circuit voltage are simply points on the I–V curve of the photovoltaic device. I_{SC} is the reverse current produced under illuminated conditions with zero volts applied. V_{OC} is the forward biased voltage required under illuminated conditions in order to achieve a delivered current of 0 A.

The maximum power delivered is the maximum of the product of the currents and voltages on the I–V curve of the photovoltaic device. The fill factor is the ratio of the maximum power point to the product of the open circuit voltage multiplied by the short circuit current. The series resistance is the resistance observed at relatively high current under forward bias and can be found by taking the slope of the I–V curve at voltages significantly higher than the open circuit voltage (i.e. 2–3 V).

In addition to these figures of merit, organic photovoltaics also have the disadvantage that their operating lifetimes are relatively short [21]. Device performance as a function of time is therefore a more critical parameter when considering organic or hybrid photovoltaic devices as opposed to inorganic photovoltaic devices. This aspect of polymer–based photovoltaics is not explored in this work, but is crucial to the evolution of these devices from strictly research oriented into a consumer application.

CHAPTER 4
Experimental Procedure

The fabrication procedure for the devices discussed in this thesis involve several steps as shown in figure 4–1. Also shown are some of the typical measurements done on the device for characterization. Each of these steps are discussed in detail in the following sections.

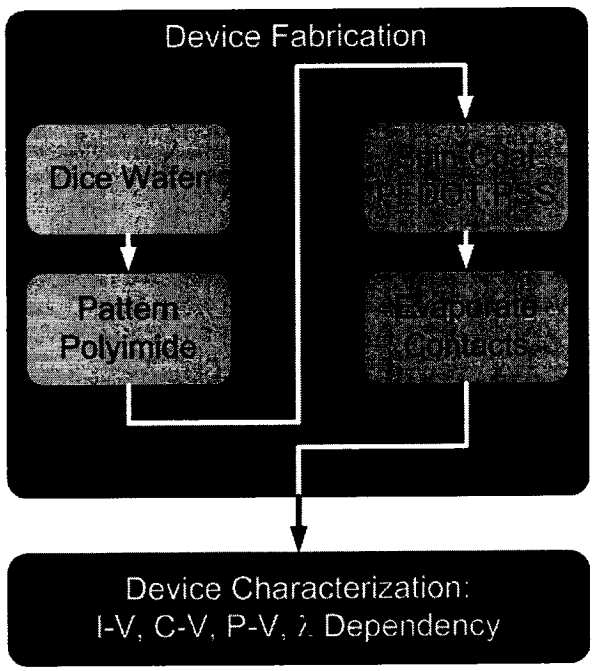

Figure 4–1: Flow chart showing the main steps in the fabrication process for the hybrid heterojunction.

4.1 Wafer Preparation

A 2–inch n–type <111> silicon wafer with listed resistivity of between 3–6 $\Omega \cdot cm$ ($1 \times 10^{15}\ cm^{-3}$) is diced into six pieces using a hand held diamond scribe as shown in figure 4–2.

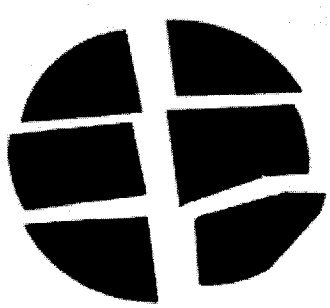

Figure 4–2: Diced 2-inch n-type silicon wafer.

Each piece is then placed in a buffered HF solution ($H_2O : NH_4F : 49\%HF = 170 : 113 : 26$ by weight) for no longer than 20 seconds to remove any residual oxide or other surface impurities. The wafer is then immersed into de-ionized water for a period of approximately 5 minutes with the water being replaced at least twice. The wafer is then spun at 3000 RPM for 25 seconds followed by a 5 minute bake at 90°C in order to ensure complete wafer dryness while avoiding the growth of a thermal oxide layer.

4.2 Polyimide Processing

The individual samples require a passivation layer that is immune to the etching effects of several common etchants like buffered HF and diluted HF solutions. Such a layer can be fabricated using polyimide, a polymer that is photosensitive and can

thus be directly patterned similar to common photoresists. The polyimide patterning procedure is as follows:

1 Warm up polyimide to room temperature by placing the bottle in luke warm bath for approximately 20 minutes. When at room temperature, the viscosity of the polyimide should be similar to honey.

2 Apply the polyimide with the narrow end of a glass pipette and spread it to cover the entire sample.

3 Spin sample at 4000 RPM for 1 minute at an acceleration of 4000 RPM/s. This should provide a final polyimide thickness of approximately 6-7 μm.

4 Bake sample at 50°C for 90 minutes. Check the samples after 20 minutes. If air bubbles have formed, reapply polyimide and spin again.

5 Prepare developer, rinse and overlap solutions as follows:

- Developer: Pyralin DE9040 commercial polyimide developer
- Rinse: N-Butylacetate
- Overlap: Developer/Rinse = 1/1

6 Expose sample through photo mask (such as the one shown in figure 4–3) under high intensity UV lamp for 5 minutes. The photo mask used can produce 3 patterned samples simultaneously as can clearly be seen from figure 4–3.

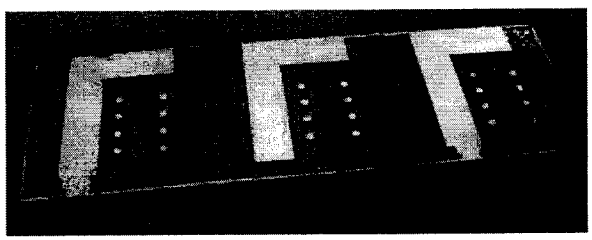

Figure 4–3: Photo mask used to create 8 circular devices per sample.

7 Develop sample in developer for 4 minutes.

8 Place sample in overlap for 30 seconds.

9 Rinse sample in rinse for 60 seconds.

10 Spin dry sample at 3000 RPM for 20 seconds. Do not rinse sample in water.

11 Examine sample under optical microscope. If polyimide has not completely been removed from the unexposed areas, repeat develop/overlap/rinse steps scaled down to 30 second long developing times until sample is fully developed.

12 Once fully developed, bake sample at 220°C for at least 2 hours.

The final, patterned polyimide can be seen in figure 4–4. Note that there are 8 exposed circles of n-type silicon that will become the 8 hybrid heterojunction devices. There is also some exposed silicon at the edges of the sample that will be used to make the contact to the n-type terminal of the junction in the next section of the fabrication process.

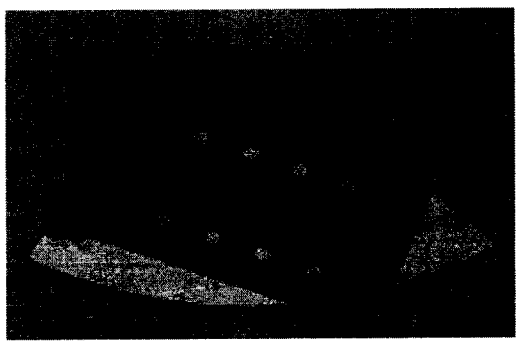

Figure 4–4: Sample after polyimide patterning.

4.3 Hybrid Organic/Inorganic Heterojuction Fabrication

The samples with patterned polyimide can now be fabricated into a hybrid organic/inorganic p-n heterojunction. The procedure is as follows:

1 Place sample in buffered HF solution for 20 seconds to reduce the presence of unwanted surface states and any thin thermal oxide that may have grown during the polyimide curing process.

2 Immerse sample in de-ionized water for 10 minutes, replacing the water twice to ensure that no buffered HF remains on the sample.

3 Spin dry sample at 3000 RPM for 20 seconds.

4 Bake dry sample at 90°C for 5 minutes

5 Place bottle of conductive grade PEDOT:PSS (Aldrich 483095) in ultrasonic bath for 5 minutes.

6 Spin conductive grade PEDOT:PSS onto sample at 2000 RPM for 25 seconds. It should be noted that other spin speeds were also tested and are reported in this document.

7 Bake samples at 110°C for 2 minutes. More time may be required for samples where a slower spin speed was used for the application of the PEDOT:PSS.

4.4 Contact Placement

Following the curing of the PEDOT:PSS, the samples should be placed immediately into an evaporation chamber to avoid environmental contamination of the exposed PEDOT:PSS surface. The sample is suspended upside-down with a shadow mask fixed to its front so that the openings in the mask align with the polyimide windows created in the polyimide patterning process. Figure 4–5 shows the shadow mask. Note that the openings are counter-bored on one side to reduce the effect of shadowing during the evaporation process.

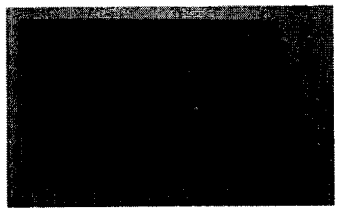

Figure 4–5: Shadow mask used for gold contact evaporation.

The sample and shadow mask are held together using alligator clips. The sample is suspended at a distance of approximately 9.5 cm (d in equation 4.2) above the heating boat (± 5 mm) into which a mass of 14 mg (m in equation 4.2)of gold (± 1 mg) will be loaded.

$$T_{Au} = \frac{V_{Au}}{SA_{hemisphere}} \tag{4.1}$$

In equation 4.1, T_{Au} is the thickness of the gold film deposited onto the sample, V_{Au} is the volume of gold placed into the boat, and $SA_{hemisphere}$ is the surface area of the hemisphere of deposition whose radius is the distance from the boat to the sample.

$$T_{Au} = \frac{m_{Au}}{\rho_{Au} \cdot 2\pi d^2} \tag{4.2}$$

In equation 4.2, d is the distance from the boat to the sample, m_{Au} is the mass of gold placed into the boat, and ρ_{Au} is the density of gold (19.32 g/cm). Taking into account the possible variations in both the distance between the boat and the sample as well as the mass of gold used, the thickness of gold used to form the top contact ranges between 10.7 nm and 15.3 nm with a nominal value of 12.8 nm. Gold

of this thickness is semi-transparent, allowing light to pass through and be absorbed by the PEDOT:PSS and n-type silicon. Unfortunately, this thickness is too thin to which to apply a needle probe for testing purposes. The needle will punch through or scrape away this thin layer of gold, thus rendering it useless. In order to combat this, a thicker contact that touches the thin layer of gold but does not cover the window through the polyimide is fabricated.

The thick gold contact can be created using the same shadow mask as in figure 4–5. Again, the shadow mask is placed in contact with the sample. The shadow mask is aligned such that a portion of each of the thin gold contacts can be seen through the holes, but so that the actual window through the polyimide is covered. The sample is again placed in the evaporation chamber, this time with an amount of gold roughly 10 times the amount used in the thin gold layer evaporation, yielding a layer of gold 10 times thicker than the semi-transparent gold contact. The probe needle can now be applied to the thick gold contact without fear of damaging either the gold layer or the hybrid heterojunction underneath.

Now that the contact to the p-type organic side of the heterojunction has been established, it is necessary to create a contact to the n-type silicon side. There should be a portion of the sample that has exposed silicon with some PEDOT:PSS on it, but no gold. Using a wooden q-tip dipped in acetone, rub away a small region of PEDOT:PSS in order to leave an exposed piece of silicon. Take a soldering iron and heat it up to the point that it can melt Wood's metal. Touch the soldering iron to the Wood's metal so that the tip of the iron is holding a small liquid bubble of

metal. Touch the bubble to the exposed region of silicon and wait a few seconds for the Wood's metal to cool and solidify. The negative contact is now created.

The final, fully fabricated device can be seen in figure 4–6. The negative Wood's metal contact can be seen near the top of the figure. The thin layer of gold can be seen to be covering the windows in the polyimide, while the thick layer of gold can be seen making contact with them, thus forming the full hybrid heterojunction.

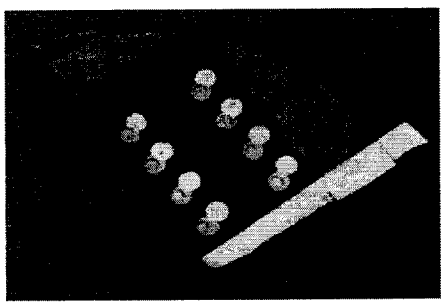

Figure 4–6: Fully fabricated hybrid heterojunction sample.

4.5 I-V Measurements

The sample is placed on a stage at a distance of 3 *cm* from a xenon lamp with a manual shutter. One needle probe is applied to the Wood's metal contact. A second needle probe is applied to the gold contact of one of the devices on the sample as can be seen in figure 4–7.

The two needle probes are plugged into an HP4145A Semiconductor Parameter Analyzer (by Hewlett Packard) through an HP16058A Test Fixture (also by Hewlett Packard) as can be seen in figure 4–8. The HP4145A is interfaced to a PC through a GPIB interface card in order to capture the acquired data.

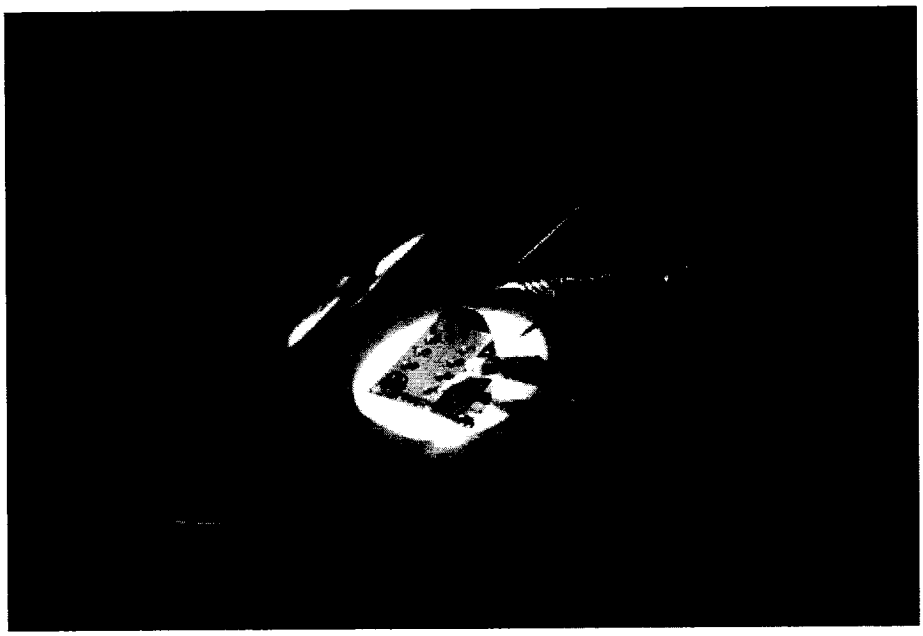

Figure 4–7: Sample with needle probes under the xenon lamp.

The I-V measurements are conducted twice for each device, once on a rough scale (0.1 V step size) from -3 V to 3 V and once on a fine scale (0.02 V step size) from -1 V to 1 V. For each measurement, the parameter analyzer acquires the same data 3 times: once with the shutter of the xenon lamp closed, once as the shutter is being opened and once with the shutter open. The light of the xenon lamp can be seen shining on the sample during the third data acquisition with the shutter open in figure 4–7. The middle data set is discarded, and the first and third data sets are used to analyze the dark and illuminated I-V characteristics of the device respectively.

Each sample has 8 devices, thus for every set of conditions measured, there are 8 dark and 8 illuminated sets of data. A device is considered to be working if it is

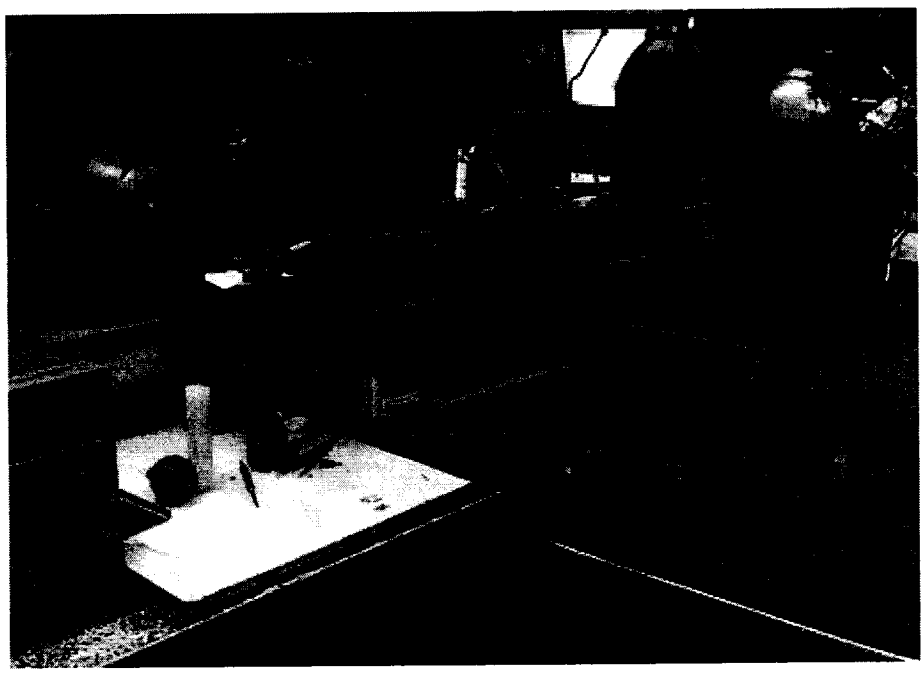

Figure 4–8: I-V measurement setup showing xenon lamp, stage, needle probes, test fixture and parameter analyzer.

capable of current rectification under dark conditions. Any devices that do not meet this criteria are excluded from the data analysis. The devices that are deemed to be working have their data at any given voltage added and then divided by the number of working devices, thus giving an average performance of devices on a given sample.

The two distinct sets of measurements are necessary to determine different critical parameters. The dark I-V characteristics from $-3\ V$ to $3\ V$ are used to determine the series resistance exhibited by a given sample. This series resistance can be ascertained by calculating the slope of the I-V curve at large forward bias voltages. The open circuit voltage, short circuit current, maximum power point and fill factor are all calculated using the illuminated I-V curve on the $-1\ V$ to $1\ V$ scale.

The open circuit voltage is approximated by finding the equation of a straight line (of the form $I = mV + b$) that passes through the last point that has a current less than zero and the first point that has a current greater than zero. The equation of this line is then evaluated for a current of 0 A as can be seen in equations 4.3–4.5.

$$m = \frac{I_{>0} - I_{<0}}{V_{>0} - V_{<0}} \tag{4.3}$$

$$b = I_{>0} - m \cdot V_{>0} \tag{4.4}$$

$$V_{OC} = -b/m \tag{4.5}$$

In equations 4.3–4.5, $I_{<0}, I_{>0}, V_{<0}, V_{>0}$ represent the largest current less than $0A$, the smallest current greater than 0 A, the voltage at the largest current less than 0 A and the voltage at the smallest current greater than 0 A respectively. The m represents the slope of the line connecting the two points and b represents the I-axis intercept of the straight line passing through the two points. V_{OC} in equation 4.5 is evaluated at $I = 0$.

The short circuit current, I_{SC} is the current measured for the one data point per data set where the condition in equation 4.6 is met:

$$|V| < 10^{-3}V \tag{4.6}$$

The power output is calculated by multiplying the negative current and voltage at every data point and plotting that against the voltage at every data point. The point at which the power is maximized is called the maximum power point as shown in equation 4.7.

$$MPP = max\{-I_X \cdot V_X\} \tag{4.7}$$

Where the subscript 'X' indicates the index of a given data point (i.e. when $X = 1$, the power is found by multiplying the first current data point by the first voltage data point).

Another critical performance parameter for a solar cell is the fill factor. It is computed according to equation 4.8 below.

$$FF = -\frac{MPP}{I_{SC} \cdot V_{OC}} \tag{4.8}$$

4.6 Capacitance Measurements

In order to acquire a better idea of what is happening at the interface between the organic and inorganic layers of the junction, capacitance-voltage measurements are undertaken. The measurements are taken by mounting the sample on the same stage that was used in the I-V measurements and applying the probe needles onto the appropriate contacts as seen previously in figure 4–7, although for C-V measurements, the xenon lamp is turned off. The probes are soldered to wires that are plugged into an HP16047A test fixture. This test fixture then connects to the HP4274A multi-frequency LCR meter. The bias that is applied to the sample in order to extract the C-V data is controlled through an HP16023B bias controller that is plugged into the back of the LCR meter. The actual applied bias voltage is then monitored through an HP34401A multimeter that is also plugged into the back of the LCR meter.

In order to take a measurement, the desired voltage is set on the bias controller and the actual voltage output from the LCR meter is read from the multimeter. The LCR meter is set to the desired output frequency and amplitude and the capacitance value is read from the it. The measurement is repeated for 4 different frequencies (100 Hz, 1 KHz, 10 KHz and 100 KHz) at a range of voltages from approximately -2.55 V to 0.85 V. They are then plotted as $\frac{1}{C^2}$ versus V because of equations 4.9-4.10.

$$C_J = \frac{\epsilon_0 K_S A}{W} \tag{4.9}$$

$$= \frac{\epsilon_0 K_S A}{\sqrt{\frac{2\epsilon_0 K_S}{q}(V_{bi} - V_A)\frac{N_A + N_D}{N_A N_D}}} \tag{4.10}$$

In equations 4.9 and 4.10, C_J is the junction capacitance, K_S is the relative permittivity, ϵ_0 is the permittivity of free space, A is the cross-sectional area of the junction and W is the width of the depletion region. Furthermore, V_{bi} is the built-in voltage of the junction, V_A is the applied voltage and N_A and N_D are the acceptor and donor concentrations respectively.

4.7 Wavelength Dependency

The conversion of light into electrical energy varies with the wavelength of light incident on the photocell. In order to explore this wavelength dependency of energy conversion, an experiment is set up as shown in figure 4–9.

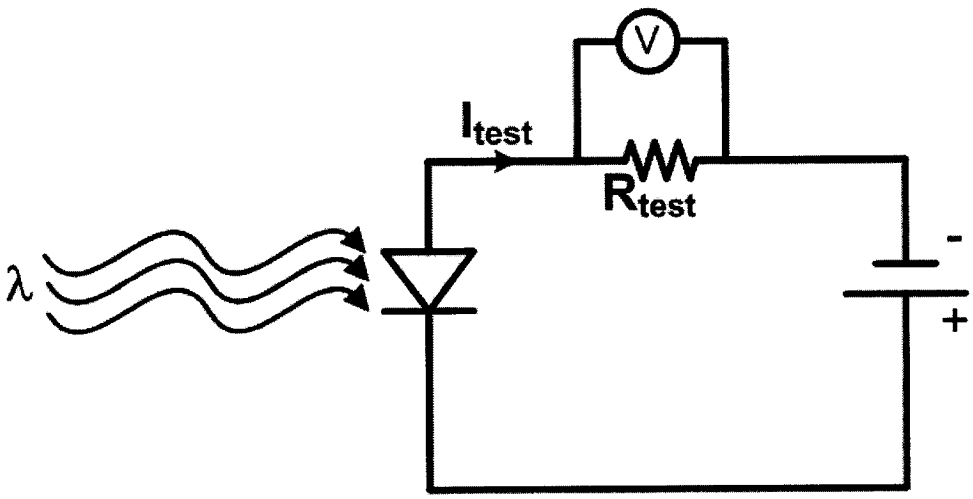

Figure 4–9: Electrical circuit diagram of wavelength dependency experiment.

A reverse bias is applied to both the hybrid heterojunction and the Schottky device in series with a large resistor across which the voltage is measured to determine the reverse bias current due to illumination at a given wavelength. For every measured wavelength using the hybrid heterojunction or the Schottky device as the photodetector, a similar measurement is undertaken using a calibrated photodetector in order to normalize the readings.

The reverse bias is applied through a standard alkaline battery, size D. The resistor is nominally 100 $K\Omega \pm 5\%$ (actual measured value is 97.5 $K\Omega$). The voltage across the resistor is measured using an HP34401A digital multimeter. The contacts are made by soldering a very thin wire to the gold p-type contact using a small amount of Wood's Metal and by soldering a thin wire to the Wood's Metal n-type contact.

Figures 4–10(a) and 4–10(b) show the overlap between the beam of light emitted from the spectrophotometer and the active area of the calibrated photodetector. Figure 4–10(a) shows the best-case scenario, where the maximum area of the photodetector is covered by the beam of light. This area, essential to know for power density calculations, is 0.12 cm^2. Figure 4–10(b) shows the worst-case scenario, where the beam from the spectrophotometer is slightly shifted relative to the active area of the photodetector. In this case, the area of overlap is 0.10 cm^2. Since the alignment of the calibrated photodetector with the spectrophotometer is done by visual inspection, the exact value of overlap is not known, and thus is just taken to be the average of these two values, namely 0.11 cm^2.

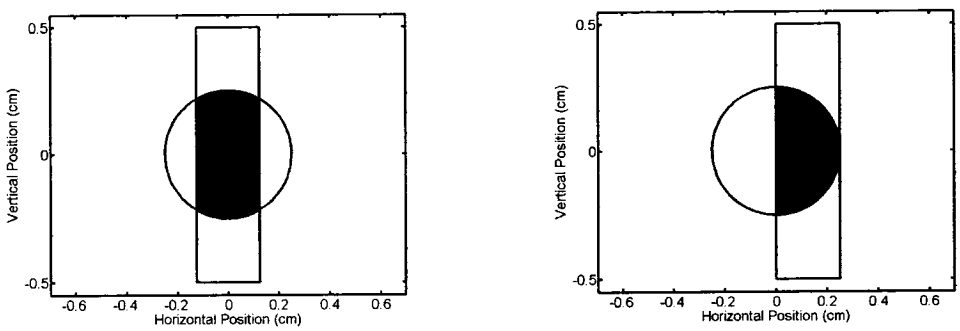

(a) Ideal Overlap

(b) Non-Ideal Overlap

Figure 4–10: Overlap between output light beam from the spectrophotometer (rectangle) and calibration device area (circle).

A Beckman DU spectrophotometer (Model 2400) in conjunction with an Oriel tungsten lamp operated at 10 V AC is used to vary the wavelength of light incident on the sample. The sample is placed at a distance of 1 cm from the output lens of the spectrophotometer.

The spectrophotometer experimental test data can be used to accurately predict the total reverse bias current in the fabricated hybrid heterojunction and Schottky devices.

Using the measured current on the calibrated photodetector at wavelengths from 350 nm to 1100 nm in increments of 25 nm as well as a predetermined responsivity (in A/W) table, the incident luminous power at each wavelength increment emitted from the spectrophotometer can be determined as shown in equation 4.11.

$$P_{incident}(\lambda) = \frac{I_{Calib}(\lambda)}{R_{Calib}(\lambda) \cdot A_{overlap}} \tag{4.11}$$

Here $P_{incident}$ represents the incident power density of a given wavelength, I_{Calib} represents the current passing through the calibration test circuit under illumination at a given wavelength, R_{calib} represents the responsivity of the calibrated photodetector at a given wavelength, and $A_{overlap}$ is the area of overlap between the active area of the calibrated photodetector and the output beam of the spectrophotometer.

Using the $P_{incident}$ calculated in equation 4.11 in conjunction with the current measured in both the Schottky and hybrid devices, we can determine their respective responsivity curves. Equations 4.12 and 4.13 show how the responsivity curves are determined. The active area in the devices is a circle of diameter 0.13 cm.

$$R_{Schottky}(\lambda) = \frac{I_{Schottky}(\lambda)}{P_{incident}(\lambda) \cdot A_{Schottky}} \tag{4.12}$$

$$R_{Hybrid}(\lambda) = \frac{I_{Hybrid}(\lambda)}{P_{incident}(\lambda) \cdot A_{Hybrid}} \tag{4.13}$$

Upon determining the responsivity curves of the Schottky and hybrid devices, it becomes necessary to analyze the spectrum of the Xenon lamp used to do the I-V characterization. Figure 4–11 (modified from [23]) shows the xenon emissions spectrum normalized to the maximum emissions point.

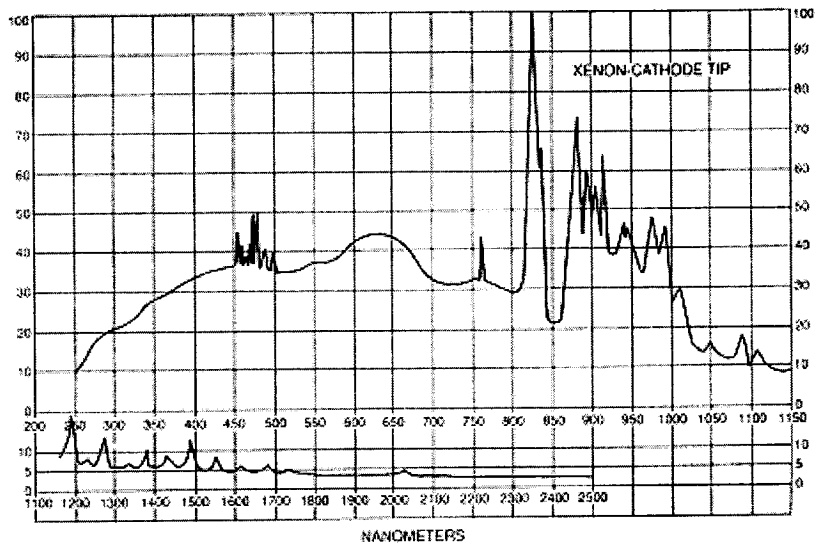

Figure 4–11: Emissions spectrum of a xenon lamp.

Figure 4–11 is integrated in order to determine the total emissions over all wavelengths of interest (namely 350 nm to 1100 nm), and the contribution from each interval of wavelength is divided by the total emissions in order to get a percentage of the total emitted power for each interval. Equation 4.14 clarifies this concept further.

$$P_{Xe-interval}(\lambda) = \frac{\int_{\lambda_i}^{\lambda_{i+1}} \sigma_{Xe}(\lambda)d\lambda}{\int_{350nm}^{1100nm} \sigma_{Xe}(\lambda)d\lambda} \tag{4.14}$$

In equation 4.14, the limits on the integral in the numerator simply imply adjacent points, $25nm$ apart from the emissions spectrum. For example, the total percentage ($P_{Xe-interval}$) of power contributed by the 350 nm to 375 nm range of the xenon lamp is calculated by finding the area under the emissions curve ($\sigma_{Xe}(\lambda)$) between 350 nm and 375 nm and dividing that by the area under the curve from 350 nm to 1100 nm.

The normalized current through the calibrated photodetector can now be determined for each wavelength range by relating the normalized power output by the xenon lamp for each wavelength range with the responsivity of the calibrated photodetector. Equation 4.15 clarifies this concept.

$$I_{Xe-normalized}(\lambda) = P_{Xe-interval}(\lambda) \cdot R_{Calib}(\lambda) \tag{4.15}$$

With the proportion of current due to each wavelength range now known, it can be integrated and related to the actual total measured current under reverse bias under the xenon lamp. This relationship is called the Lamp Power Ratio (LPR) as shown in equation 4.16.

$$LPR = \frac{\int_{350nm}^{1100nm} I_{Xe-normalized} d\lambda}{I_{Calib-Xe-measured}} \tag{4.16}$$

The Lamp Power Ratio provides the mechanism to un-normalize the current due to the xenon lamp.

$$I_{Calib-Xe}(\lambda) = \frac{I_{Xe-normalized}(\lambda)}{LPR} \tag{4.17}$$

In equation 4.17, $I_{Calib-Xe}$ represents the amount of current expected to flow through the calibrated photodetector due to illumination from the xenon lamp. Knowing this information, it is now possible to determine the actual power delivered by the xenon lamp for various wavelengths, as shown in equation 4.18.

$$P_{Xe-incident}(\lambda) = \frac{I_{Calib-Xe}(\lambda)}{R_{Calib}(\lambda) \cdot A_{overlap}} \cdot A_{Schottky/Hybrid} \tag{4.18}$$

Note that in equation 4.18, $A_{Schottky/Hybrid}$ represents the active area of either the Schottky device or the hybrid heterojunction device. The area is the same for either device since they are both fabricated using the same windows through the polyimide passivation layer.

Using all the information gathered above, the total current to be produced by the Schottky device and hybrid heterojunction under xenon lamp illumination can be predicted. Equations 4.19 and 4.20 indicate the final step in predicting the current passing through the fabricated devices.

$$I_{Xe-Schottky} = \int_{350nm}^{1100nm} P_{Xe-incident}(\lambda) \cdot R_{Schottky}(\lambda) d\lambda \tag{4.19}$$

$$I_{Xe-Hybrid} = \int_{350nm}^{1100nm} P_{Xe-incident}(\lambda) \cdot R_{Hybrid}(\lambda) d\lambda \tag{4.20}$$

The direct comparison between the current expected from the preceding mathematical analysis and the measured current at a reverse bias of 1.5 V under xenon lamp illumination can be found in the Experimental Results chapter.

CHAPTER 5
Experimental Results

5.1 Samples Analyzed

The devices discussed in this chapter consist of several different structures. The different structures have been assigned a sample number to facilitate ease of discussion and characterization. Table 5–1 provides of the sample number, fabrication date, device structure, any pertinent fabrication notes and the number of devices per sample discussed. All data reported for a given sample is averaged over the number of working devices on that sample unless otherwise noted. Note that Wood's Metal is specified simply by WM.

Table 5–1: Sample reference numbers

No.	Date Fabricated	Device Structure	Notes	No. Devs.
1	2006/04/24	WM/n-Si/PEDOT(2000 RPM)/Au	BHF treatment	8
2	2006/05/02	WM/n-Si/Au	BHF treatment	8
3	2006/04/21	WM/n-Si/PEDOT(500 RPM)/Au	BHF treatment	8
4	2006/04/21	WM/n-Si/PEDOT(1000 RPM)/Au	BHF treatment	3
5	2006/04/24	WM/n-Si/PEDOT(4000 RPM)/Au	BHF treatment	7
6	2006/04/24	WM/n-Si/PEDOT(6000 RPM)/Au	BHF treatment	5
7	2006/04/07	WM/n-Si/PEDOT(2000 RPM)/Au	untreated	1
8	2006/04/10	WM/n-Si/PEDOT(2000 RPM)/Au	BHF treatment	1
9	2006/05/02	WM/n-Si/PEDOT(2000 RPM)/Au	untreated	8
10	2006/05/02	WM/n-Si/Au	untreated	8
11	2006/05/23	WM/n-Si/Au	BHF treatment	1
12	2006/05/23	WM/n-Si/PEDOT(2000 RPM)/Au	BHF treatment	1

It should be noted also from table 5–1 that samples 7 and 8 actually had more than 1 working device each, but only one device on each was tested for C–V characteristics. These two samples were not used for I–V characterizations.

Similarly, it should be noted that samples 11 and 12 from table 5–1 had more than one working device each, but that only one device was used for spectrophotometer measurements. These two samples were not directly used for I–V characterizations.

The notes column consists of two possibilities: "BHF treatment" and "untreated". BHF treatment refers to the short treatment in a buffered HF solution of the n-Si wafer after the processing of the polyimide passivation layer. Untreated refers to leaving the n-Si wafer with processed polyimide untreated immediately before applying the PEDOT:PSS solution.

5.2 C–V Characteristics

Figure 5–1 shows the capacitance vs voltage characteristics of an untreated sample (sample 7) and a BHF treated sample (sample 8) at four different frequencies. In the legend, the '7' represents the untreated sample while the '8' represents the BHF treated sample.

Using a modified version of equation 4.10, we can arrive at some conclusions about the properties of the PEDOT:PSS layer. Equation 5.1 uses a differential version of 4.10 in order to eliminate the need to know the exact value of the built in voltage, V_{bi}.

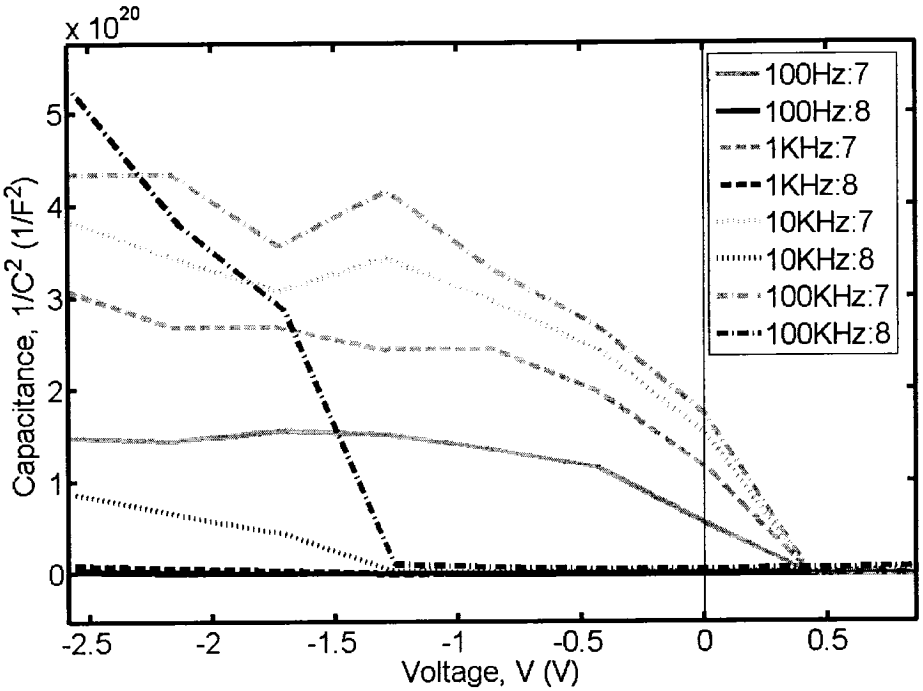

Figure 5–1: C–V characteristics of an untreated sample (sample 7) and a sample treated with BHF (sample 8)

$$\Delta(C_J) = \frac{\epsilon_0 K_S A}{\sqrt{\frac{2K_S\epsilon_0}{q}\left[\Delta\left(V_{bi} - V_A\right)\right]\frac{N_A + N_D}{N_A N_D}}} \tag{5.1}$$

Upon reorganization and simplification of equation 5.1, we arrive at equation 5.2, allowing us to determine the carrier concentration in the PEDOT:PSS.

$$\frac{N_A + N_D}{N_A N_D} = \frac{q\epsilon_0 K_S A^2}{2} \cdot \frac{\Delta\left(\frac{1}{C_J^2}\right)}{\Delta\left(-V_A\right)} \tag{5.2}$$

There are two scenarios possible here in order to simplify the calculation; namely that $N_A >> N_D$ or that $N_D >> N_A$. Equation 5.2 simplifies to either equation 5.3 for the $N_D >> N_A$ case or equation 5.4 for the $N_A >> N_D$ case.

$$\frac{1}{N_A} = \frac{q\epsilon_0 K_{PEDOT:PSS} A^2}{2} \cdot \frac{\Delta\left(\frac{1}{C_J^2}\right)}{\Delta\left(-V_A\right)} \tag{5.3}$$

$$\frac{1}{N_D} = \frac{q\epsilon_0 K_{n-Si} A^2}{2} \cdot \frac{\Delta\left(\frac{1}{C_J^2}\right)}{\Delta\left(-V_A\right)} \tag{5.4}$$

Here A is the active area of the device and is defined as the area of a circle of diameter 0.075 cm, ϵ_0 is the permittivity of free space, K_{n-Si} is the relative permittivity of silicon and has a value of 11.8, $K_{PEDOT:PSS}$ is the relative permittivity of PEDOT:PSS and is assumed to have a value of approximately 4 as with most electrically conductive polymers, and q is the charge on one electron.

Using the data from sample 7, equation 5.3 yields an N_A in the order of 10^{16} cm^{-3} while equation 5.4 yields an N_D in the order of 10^{15} cm^{-3}. Since the donor concentration of the n-type silicon, however, is known to be in the order of 10^{15} cm^{-3}, it can be concluded that the results from equation 5.3 are invalid (i.e. the assumption that $N_D >> N_A$ was shown to be incorrect).

Using the data from sample 7, we find an N_A on the order of 10^{16} cm^{-3}. Using the data from sample 8, we find an N_A on the order of 10^{20} cm^{-3}. This discrepancy can be attributed to the surface states acting as recombination centres for the untreated sample. We can approximate the density of recombination centres in the untreated sample to therefore be 10^4 cm^{-3}. Note that in a one sided junction, most of the

useful information that can be extracted comes from the less heavily doped side due to the fact that the vast majority of the depletion region lies in the lightly doped material. Considering this, the preceding analysis is not intended to provide an accurate calculation of the dopant concentration in the PEDOT:PSS, but rather to provide an initial impression of how PEDOT:PSS is far more heavily doped than the n-type silicon. In order to get an accurate number of the carrier concentration in PEDOT:PSS, further experiments would have to be conducted.

Unfortunately, this analysis does not allow for any quantitative determination of the actual value of N_A within the PEDOT:PSS, but simply a qualitative understanding that the carrier concentration, N_A, of PEDOT:PSS is much larger than 10^{15} cm^{-3}.

5.3 I–V Characteristics: Treatment

Ultimately, the performance of the device is not defined by the C–V characteristics, but rather the I–V characteristics. While we used the C–V graph to gain some insight into the behaviour of a device treated with BHF compared to one not treated with BHF, it is necessary to perform the I–V characterization to truly appreciate the worth of these two types of devices.

Figures 5–2 and 5–3 show a direct comparison of the I–V characteristics of a BHF treated sample (sample 1) and an untreated sample (sample 9) with figure 5–2 varying over a wide range of voltages in order to analyze behaviour at large forward and reverse biases and with figure 5–3 zooming into a narrow range of voltages in order to analyze the photovoltaic properties at relatively low bias.

From figure 5–2, several observations can be made. First, and most importantly, it can be seen that both samples provide a significantly larger illuminated reverse current than dark current. This proves that the samples indeed are absorbing light to produce a current. Additionally, in the forward bias direction, it can be seen that sample 1 increases very rapidly compared with sample 9. This represents the relative series resistance between the treated and untreated samples and shows that the untreated sample has a much larger series resistance than that of the BHF treated sample.

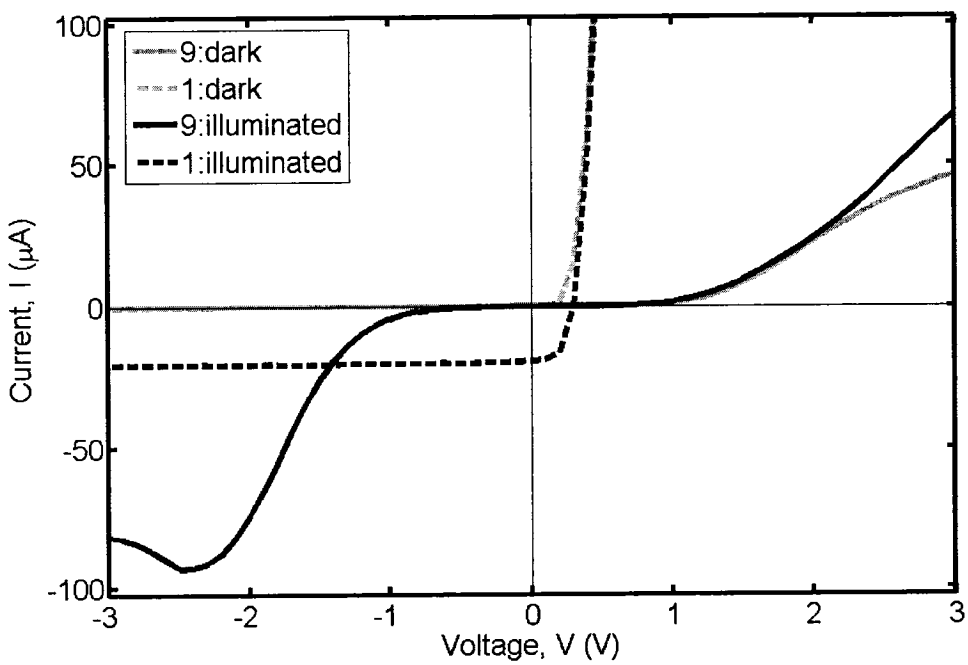

Figure 5–2: I–V characteristics of an untreated sample (sample 9) and a sample treated with BHF (sample 1) from -3V to 3V.

Additionally from figure 5–2, it can be seen that at a large reverse bias sample 9 provides a significantly larger photocurrent than sample 1. This phenomenon can be explained by modeling the surface states at the interface between the n-Si and PEDOT:PSS as a very thin barrier layer.

As the reverse bias is applied, an electric field forms in the PEDOT:PSS, in the n-Si and in the thin barrier layer. Under these conditions, when illuminated, the exciton begins to dissociate and arrives at the barrier layer with significant momentum. Upon arriving at the barrier layer, an avalanche-type multiplicative increase in current occurs throughout the thickness of the barrier layer. Because the barrier layer is very thin, the current does not increase by orders of magnitude as in the case of avalanche breakdown of a standard inorganic p–n junction, but instead can only avalanche for a short period of time; namely the amount of time it takes a carrier to cross the barrier layer.

This avalanching is different from the principle of the photomultiplier used in light–sensing applications. Photomultipliers use a strong reverse bias to enhance the current due to illumination by creating a strong electric field throughout the depletion region. Here, the excitons have the whole depletion width to multiply, thus increasing the current many times over.

Since this barrier layer does not exist in sample 1 because the BHF removed it, this current multiplication at large reverse biases does not exist, resulting in fewer carriers arriving at the contacts.

Figure 5–3 provides further insight into what is happening as the performance in a tighter voltage range is analyzed.

For sample 1, it can be seen that the curve fits an idealized curve for the photovoltaic response of a p–n junction. The photocurrent remains flat before sharply bending, indicating a good fill factor.

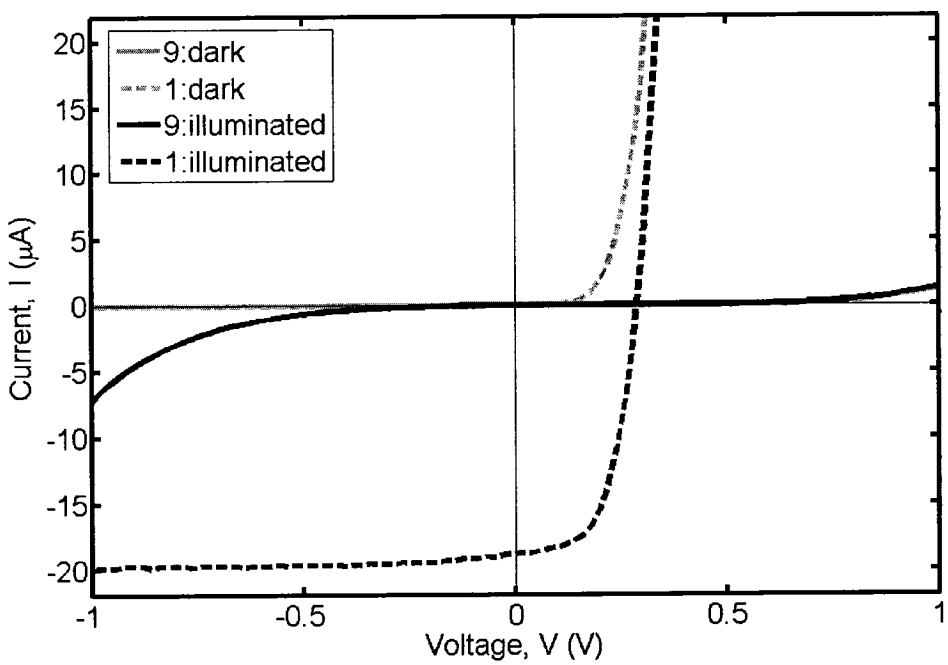

Figure 5–3: I–V characteristics of an untreated sample (sample 9) and a sample treated with BHF (sample 1) from $-1\ V$ to $1\ V$

Sample 9, however, paints a different picture. Continuing with the barrier layer model proposed above, when no significant reverse bias applied, the barrier acts to trap any excitons generated in either of the bulk regions or the depletion region. Electrons and holes arrive at the edge of the barrier layer with relatively little momentum and settle into the surface states present. Consequently, photocurrent at

zero bias is very close to zero, rendering V_{OC} and I_{SC} to be very small, and reducing the fill factor to a very small number as well (as seen in table 5–3).

This trapping of free electrons and holes by the barrier layer continues through small forward biases and requires a large forward bias to be overcome. This is clear from both figures 5–3 and 5–2 as the current remains very close to zero until nearly 1 V and remains significantly lower than that of sample 1 up to 3 V. This carrier trapping within the barrier layer also, therefore, explains the high series resistance of sample 9.

5.4 I–V Characteristics: Schottky vs. Hybrid

The performance comparison of related devices is important in deriving the relative quality of one design versus another. Figures 5–4 and 5–5 show the I–V characteristics of a hybrid heterojunction (sample 1) and a Schottky device with no PEDOT:PSS layer (sample 2). Both devices have the n-type silicon surface treated with buffered HF prior to any further fabrication steps in order to remove as many unwanted surface states as possible.

Figure 5–4 shows the illuminated I–V characteristics over a wide range of voltages (-3 V to 3 V) while figure 5–5 zooms in on the I–V characteristics over a narrow range of voltages (-1 V to 1 V) showing both the dark and illuminated conditions.

Figure 5–4 indicates that the series resistance of sample 2 is much higher than the series resistance of the sample 1 as can be seen by the variation of slopes between the two samples at large forward bias.

It is likely that the series resistance of the Schottky device (sample 2) is large not because of the physical properties of the device, but rather a defect in fabrication

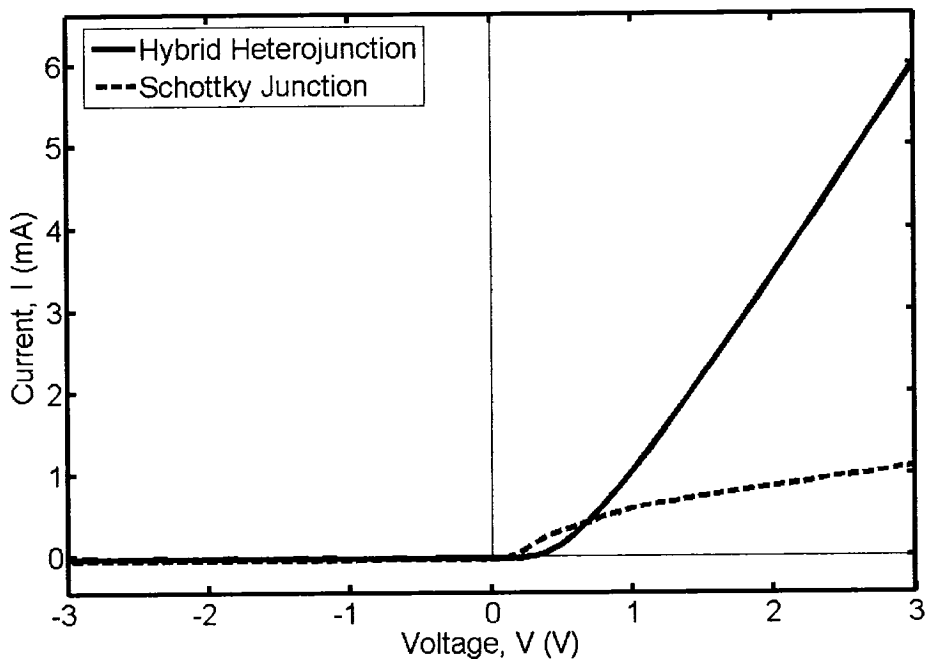

Figure 5–4: Illuminated I–V comparison of hybrid junction (sample 1) and Schottky junction (sample 2) from -3V to 3V

resulting in a non–ohmic contact. The sample contains eight devices, but every device contains a common negative terminal consisting of Wood's metal applied to the n-type silicon surface using a soldering iron. The soldering iron can create a thin oxide layer if applied slightly too long to the silicon surface, thus increasing the series resistance of the device. This cannot be confirmed or disproved by sample 11 as it was solely used for spectrophotometer data at reverse bias of 1.5 V, not I–V data.

Figure 5–5 shows that the Schottky device has a larger I_{SC} while the hybrid heterojunction has a larger V_{OC}.

The I_{SC} variation can be explained considering the junction at the PEDOT:PSS/n-Si interface. For the Schottky device, any light-generated hole needs to reach the edge of the electric field within the n-Si in order to be swept to the gold contact. Thus the hole lifetime and mobility in n-Si are the factors that dictate the ability of generated excitons to be converted into current. For the hybrid heterojunction, however, there is an additional interface present between the n-Si and PEDOT:PSS. Here, not only does the light-generated hole have to reach the edge of the electric field present within the n-Si, but also must cross the heterojunction barrier into the PEDOT:PSS. Even though the buffered HF treatment has removed many surface states, some still exist and holes can easily become trapped at this interface, thus reducing the overall current. It should also be noted that since the PEDOT:PSS is more heavily doped than the n-Si, the bulk of the depletion region lies within the n-Si, not the PEDOT:PSS. Nevertheless, the small thickness of depletion region that does lie within the PEDOT:PSS is of low mobility relative to the n-Si. Taking this into account, the holes that have managed to cross the PEDOT:PSS/n-Si interface may still recombine in this thin depletion region found within the PEDOT:PSS layer.

The V_{OC} variation can be explained using the same logic along with equations 5.5 and 5.6 [24].

Equation 5.5 simply shows how the current of the junction while illuminated takes into account both the current due to light, I_L, the saturation current, I_0 of the device as well as the voltage applied, V.

$$I = I_L - I_0 \left[e^{\frac{qV}{kT}} - 1 \right] \tag{5.5}$$

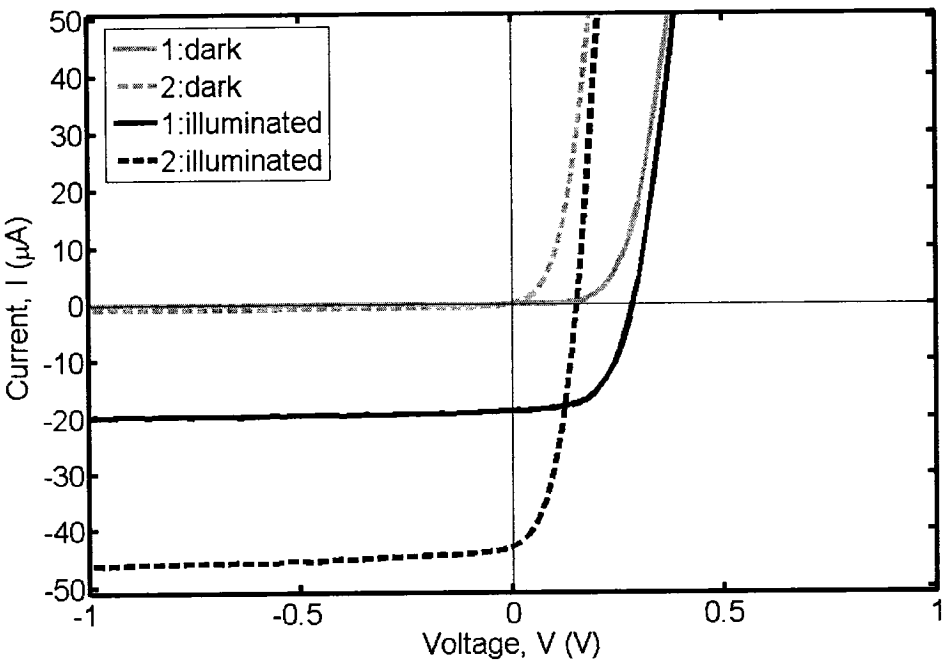

Figure 5–5: Dark and illuminated I–V comparison of hybrid junction (sample 1) and Schottky junction (sample 2) from -1V to 1V

By setting the current to zero, and solving the equation for V, we arrive at the open circuit voltage, V_{OC} as shown in equation 5.6.

$$V_{OC} = \frac{kT}{q} \ln\left(1 + \frac{I_L}{I_0}\right) \tag{5.6}$$

By comparing the reverse bias data for samples 1 and 2 in both illuminated and dark conditions, we can determine the values for I_0 and I_L. It is found that for sample 1, I_0 is approximately 29 nA while I_L is approximately 19 μA. For sample 2, I_0 is approximately 560 nA while I_L is approximately 43 μA.

Using equation 5.6, sample 1 has a theoretical V_{OC} of 0.168 V while sample 2 has a theoretical V_{OC} of 0.113 V. While these values don't quantitatively agree with the results in table 5–3, they do qualitatively show that the hybrid heterojunction provides a significantly larger V_{OC} than the Schottky device does. The discrepancy between the theoretically calculated results and the measured results comes from an over-interpreted I_0. Reorganizing equation 5.6 to solve for I_0 using the measured V_{OC} values listed in table 5–3, we arrive at equation 5.7.

$$I_0 = \frac{I_L}{e^{\frac{qV_{OC}}{kT}} - 1} \tag{5.7}$$

Using equation 5.7 with the V_{OC} value measured and listed in table 5–3, we arrive at idealized values of I_0 for samples 1 and 2 of about 0.3 nA and 120 nA, respectively. The discrepancies of these two numbers can be attributed to non-ideal factors in the fabricated devices, particularly at the interface of the PEDOT:PSS/n-Si junction of sample 1.

Equations 4.19 and 4.20 provided a framework for predicting the reverse current of samples 1 and 2 at a reverse bias of 1.5 V. The equations yielded a theoretical reverse current for samples 1 and 2 of 10.6 μA and 20.6 μA, respectively using the spectrophotometer data obtained using samples 11 and 12. Samples 1 and 2 are not used for spectrophotometer characterization because, being exposed to the environment, their performance would have changed in the weeks between fabrication and characterization. The measured current values according to the data used to produce figure 5–4 for a reverse bias of 1.5 V are 20.2 μA and 42.3 μA for samples 1 and 2, respectively.

The variation between the theoretical current values calculated on spectrophotometer data from samples 11 and 12 compared to measured current values on samples 1 and 2 can be due to a large number of factors, from environment to variations in material parameters, although most likely, the thin gold window used as the front contact of the devices on samples 11 and 12 were slightly thicker than on samples 1 and 2, resulting in slightly less light arriving to the active layers. What should be noted, however, is that the approximate 2:1 ratio of reverse Schottky current to reverse heterojunction current is observed both using direct measurement (samples 1 and 2) as well as in calculations based on spectrophotometer measurements.

It should be noted that direct comparison between theoretical and measured values for samples 11 and 12 or samples 1 and 2 were not conducted due to the rapid degradation of performance of these sampes caused by exposure to the environment. This issue is discussed briefly in the Future Work section.

Using the data from figure 5–5, it is also possible to calculate the fill factor. Sample 1 shows a fill factor improvement of 29% when compared to sample 2 as summarized in table 5–3. This can be largely attributed to the increase in V_{OC}.

5.5 I–V Characteristics: PEDOT:PSS Thickness

The role of the PEDOT:PSS layer in the I–V characteristics of the hybrid heterojunction can be better understood by varying its thickness. In order to vary the thickness of the polymer layer, the spin coater is operated at different spin speeds, but for the same amount of time. The formula relating spin speed and polymer thickness can be seen in equation 5.8 [25].

$$T = \frac{KC^{\beta}\eta^{\gamma}}{\omega^{\alpha}} \tag{5.8}$$

In equation 5.8, T refers to the polymer thickness, K is an overall calibration constant, C is the polymer concentration in grams per 100 ml solution, η is the intrinsic viscosity, ω is the spin speed in rotations per minute and β, γ and α are experimental constants.

Since K, C and η are constant for every spin speed used, we can consider that T varies inversely with ω^{α}. It should also be noted that α ranges from 1 (considering zero evaporation during spinning) to 0.5 (considering an evaporation rate that varies with $\omega^{0.5}$ as with most applications). Evaporation is considered here, thus α is chosen to have a value of 0.5.

Figure 5–6 shows the cross-section of PEDOT:PSS spun onto an n-Si wafer and covered with evaporated aluminum for mechanical stability. The sample was placed in an SEM and observed at an angle of 45°. Sharp focus could not be achieved, but considering best and wost case scenarios, the thickness is observed to be approximately 530 ± 70 nm after adjusting for the 45° viewing angle.

Knowing this thickness, it is possible to arrive at an approximate value for the thickness of the other PEDOT:PSS thicknesses measured using the relationship $T \sim \omega^{-0.5}$. These values are listed in table 5–2.

Figures 5–7 and 5–9 show how the illuminated I–V characteristics change with PEDOT:PSS spin speed.

Figure 5–7 shows the performance of samples 1, 3, 4, 5 and 6 from -3 V to 3 V under illuminated conditions. The series resistance can be inferred from the slope

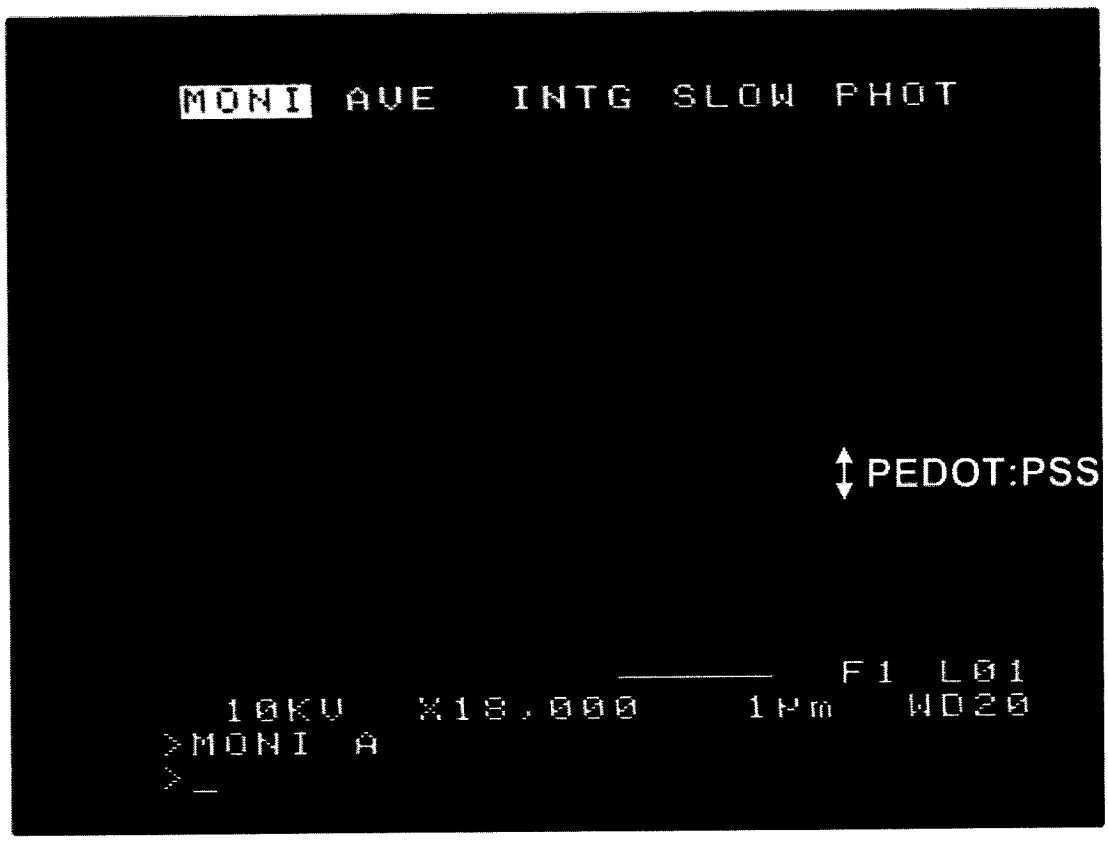

Figure 5–6: Cross section of n-Si/PEDOT:PSS/metal for PEDOT:PSS spun on at 2000 RPM as seen from SEM.

of the I–V curves at high forward biases. It can be seen that the series resistance at 2000 RPM is the lowest, while the series resistance is highest at 500 RPM.

Figures 5–8(a), 5–8(b) and 5–8(c) show the current paths flowing through the devices illustrating how different PEDOT:PSS thicknesses influence the flow of current.

The high series resistance of sample 3, depicted in figure 5–8(a), can be explained by the number of inter-molecular "jumps" that electrons must make in order

Table 5–2: Speed to thickness calibration table.

Spin Speed (RPM)	Thickness (nm)	Notes
500	1060	calculated
1000	750	calculated
2000	530	measured on SEM
4000	375	calculated
6000	300	calculated

to traverse the PEDOT:PSS region. As was previously explained, carriers can relatively easily move along the polymer backbones, but have difficulty moving from one polymer molecule to the next, thus thick polymer layers result in high resistance. In order for the current to go from the n-Si to the thin gold window, it must first cross a relatively long, resistive PEDOT:PSS thickness

On the other hand, series resistance is also high for samples 5 and 6, depicted in figure 5–8(c), compared with sample 1. This indicates that having a very thin polymer layer can also result in high series resistance. Here the conductive bottleneck occurs in the window layer of thin gold. The thin layer of gold is forced to conduct almost all of the current through the device as the cross-sectional area of the polymer is so small that its resistance becomes very large.

The lowest series resistance case is found in figure 5–8(b), representing sample 1. Here, the thin gold window, having a relatively high resistance, is in parallel with a PEDOT:PSS layer of sufficient cross–sectional area to conduct some non–trivial amount of current. These two resistances in parallel, reduce the overall resistance of the device compared to either the thin or thick PEDOT:PSS layer conditions.

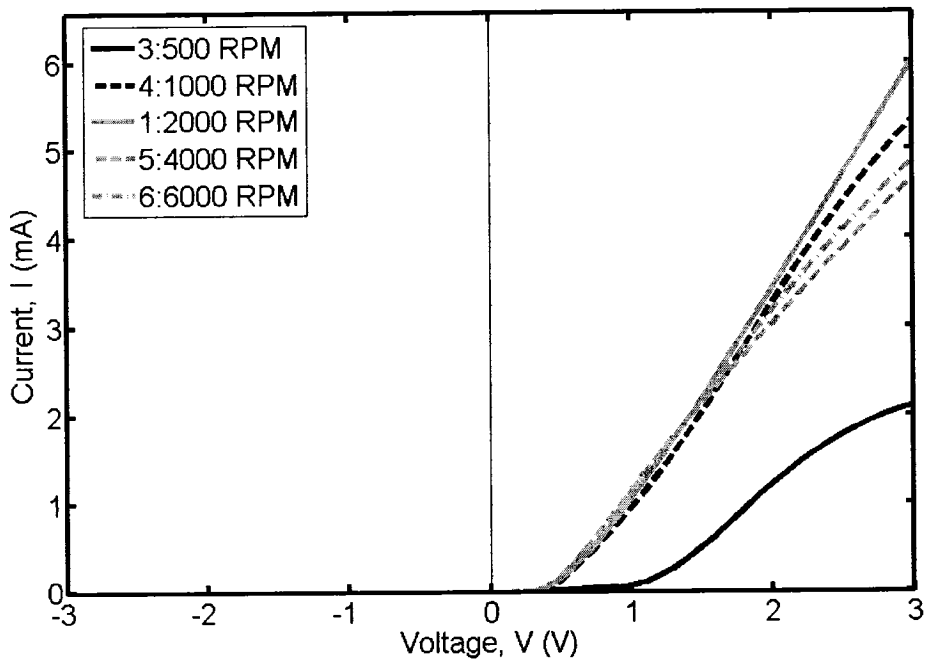

Figure 5–7: Illuminated I–V characteristic comparison of hybrid junctions at different PEDOT:PSS thicknesses (samples 1, 3, 4, 5 and 6) from -3V to 3V

Figure 5–9 shows the variation in I–V characteristics of samples 1, 3, 4, 5 and 6 over the range of $-0.2\ V$ to $0.4\ V$ under illuminated conditions. Dark characteristics are not provided in order to prevent the figure from becoming too cluttered. Not surprisingly, the performance between the different samples is not radically different because it is assumed that the bulk of the light absorption is provided by the n-type silicon, while the principle role of the PEDOT:PSS layer is to aid in charge separation and charge transport.

The I_{SC} values of samples 1, 3, 4 and 5 are all relatively close to each other with sample 6 having a significantly higher I_{SC}. Considering the argument for the high

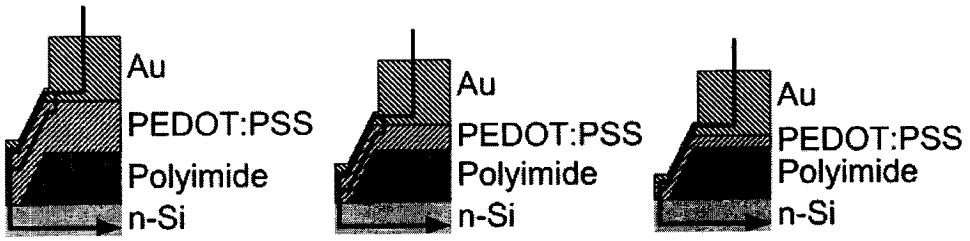

(a) Thick PEDOT:PSS layer (b) Optimal PEDOT:PSS layer (c) Thin PEDOT:PSS layer

Figure 5-8: Current paths (indicated by black arrows) through active area of devices with varying PEDOT:PSS thicknesses.

I_{SC} found in the Schottky device, it can be noted that recombination within sample 6 may be reduced due to the reduced thickness of the low-mobility PEDOT:PSS layer. This reduction in recombination can contribute to an increased I_{SC} in thin PEDOT:PSS structures.

It would further be expected that sample 3 would have a low I_{SC} due to such a thick layer of resistive PEDOT:PSS impeding the flow of current. This, however, is offset to some degree by enhanced light absorption by PEDOT:PSS due to a more than 1 μm thick polymer layer.

The V_{OC} of samples 1, 4, 5 and 6 are all within 14% of each other with sample 3 having a slightly higher value. Also considering the argument comparing the V_{OC} in samples 1 and 2 (equation 5.6), it is clear that a low I_0 contributes to higher V_{OC}. Sample 3 had the lowest I_0 followed by sample 4. Not surprisingly, they respectively provide the highest and second highest V_{OC} values. These low I_0 values can be attributed to the relatively thick PEDOT:PSS layer requiring more carrier "jumping" in order to pass a current.

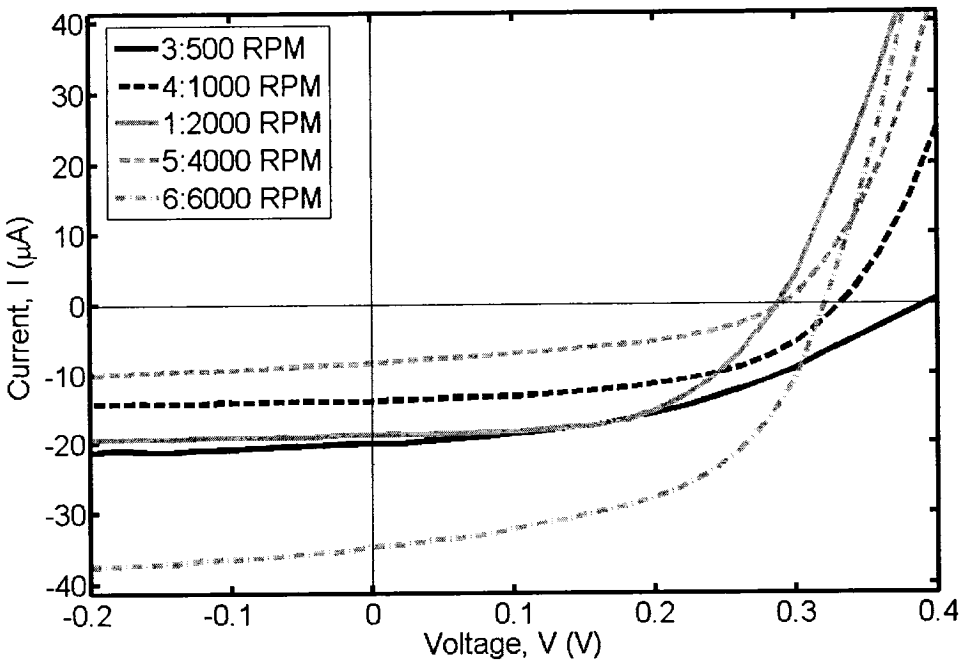

Figure 5–9: Illuminated I–V performance comparison of hybrid junctions at different PEDOT:PSS thicknesses (samples 1, 3, 4, 5 and 6) from $-0.2\ V$ to $0.4\ V$

5.6 P–V Characteristics, Fill Factor & Efficiency

No discussion of photovoltaic devices would be complete without addressing the power they are capable of producing. Figure 5–10 takes the current and voltage data from figure 5–9, multiplies them together and plots them against voltage once again in order to arrive at a power–voltage curve.

The best P–V performance is exhibited by sample 6, while the poorest is exhibited by sample 5. The reasons for the P–V characteristics varying as they do can largely be extrapolated from the arguments used to justify I–V performance.

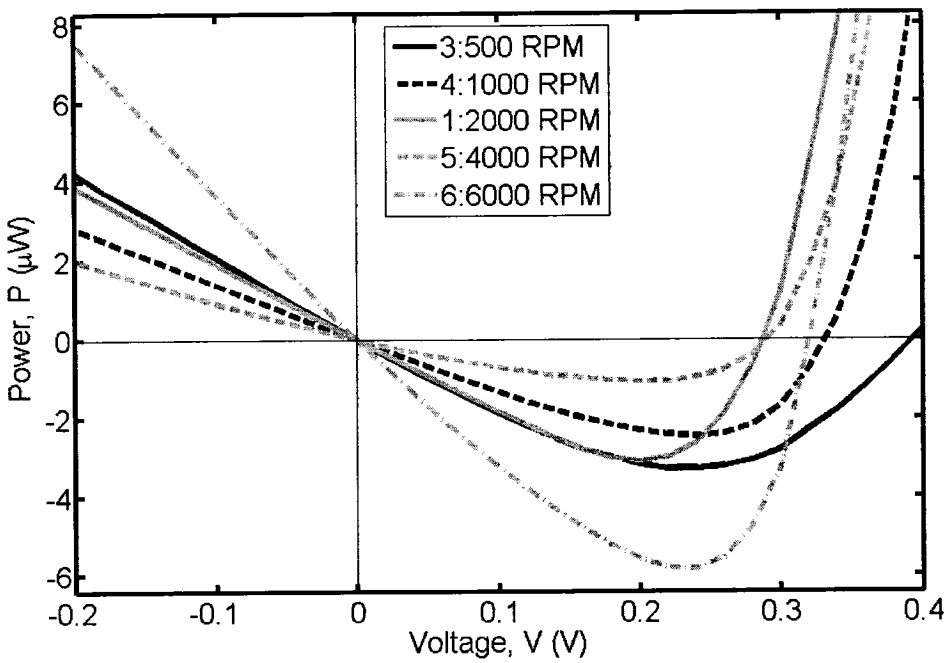

Figure 5–10: Illuminated power–voltage characteristic comparison of hybrid junctions at different PEDOT:PSS thicknesses (samples 1, 3, 4, 5 and 6) from $-0.2\ V$ to $0.4\ V$

Equation 4.8 is the mathematical interpretation of the fill factor, but it can also be interpreted graphically. The fill factor can be considered to be a measure of the "squareness" of the I–V characteristic in the fourth $+V$, $-I$ quadrant. If the characteristic is perfectly square, then the fill factor has a value of 100%, whereas the more the I–V characteristic cirves, the smaller the fill factor becomes.

Revisiting figure 5–9, it can immediately be seen that sample 1 has the most "square" I–V characteristic while sample 3 has the least "square" I–V characteristic. This interpretation becomes abundantly clear when revisiting figure 5–3. It can clearly be seen that sample 9 has an I–V characteristic that is not "square" at all.

Not surprisingly, table 5–3 shows sample 9 having the worst fill factor of all the devices tested.

The efficiency, η of the is defined as the maximum power produced by the photovoltaic device compared with the input optical power to the device as in equation 5.9.

$$\eta = \frac{P_{MAX}}{P_{IN}} \tag{5.9}$$

The data from the emissions spectrum of the xenon lamp (shown in figure 4–11) is integrated and normalized using a calibrated solar cell. In this way, the output optical power is found to be 70 mW/cm^2. It should be remembered that the emissions spectrum of the xenon lamp do not exactly match the AM0, AM1 or AM1.5 conditions, and therefore efficiency data must be analyzed with a critical eye.

Using equation 5.9 as well as a P_{IN} of 70 mW/cm^2 and a device area of 0.0133 cm^2, the efficiency of the samples can be determined. The results, seen in table 5–3 are generally of the same magnitude as those listed in the literature for hybrid heterojunction photovoltaics where the inorganic substrate is n-type silicon(table 2–1). The only exceptions involve a second inorganic layer of nano-porous silicon that is capable of enhanced light absorption, and even then, the efficiency enhancement is by less than one order of magnitude.

5.7 Summary of results

The results discussed in the previous sections of this chapter are summarized in table 5–3 and can be compared directly with the results of other devices discussed in the literature review in table 2–1.

Table 5–3: Figures of merit measured on fabricated devices

Sample	R_S (Ω)	I_{SC} (μA)	V_{OC} (V)	MPP (μW)	FF (%)	η (%)
1	388	-18.8	0.287	3.08	57.0	0.33
2	4132	-43.1	0.153	2.91	44.1	0.31
3	1724	-20.0	0.393	3.26	41.5	0.35
4	568	-13.8	0.332	2.45	53.5	0.26
5	676	-8.3	0.291	1.06	43.5	0.11
6	649	-34.8	0.320	5.83	52.3	0.63
9	52083	-0.018	0.217	5.58×10^{-4}	14.1	5.99×10^{-5}

As can be seen in table 5–3, sample 1 provides the best fill factor, indicating the most ideal shape of the I–V curve (i.e. the most "square" curve). This is the primary reason it was chosen as the hybrid device with which to compare the Schottky device.

Sample 1, however, does not provide the best data for all figures of merit. Indeed, sample 6 shows the highest efficiency and greatest maximum power produced. It also provides a high fill factor, but one slightly lower than that of sample 1.

Sample 9, on the other hand shows the poorest performance over all figures of merit. This is primarily due to the surface states at the n-Si/PEDOT:PSS interface impeding the flow of current due to illumination at small forward and reverse biases.

Overall, the hybrid heterojunction involving two active layers (n–type silicon and p–type PEDOT:PSS) compares well with other devices fabricated involving two active layers where the inorganic material is n–type silicon; namely [5], [6], [8] and [9].

CHAPTER 6
Additional Work

An involved future undertaking for the topics covered in this present work involve adding a layer of nano–porous silicon between the n–type silicon layer and the p–type PEDOT:PSS layer. As mentioned previously, this additional layer would provide enhanced light absorption at different wavelengths than those already absorbed by monocrystalline silicon. Some aspect of this additional work has been attempted and is here documented.

A procedure for producing nano–porous silicon on a silicon substrate is as follows:

1 Pattern polyimide as described in chapter 4.

2 Apply Wood's metal as described in chapter 4.

3 Prepare a diluted HF:H_2O solution of relatively high $wt.\%$ concentration (i.e. $> 10\%$).

4 Immerse sample into HF:H_2O solution, keeping the Wood's metal outside of the liquid and connecting it to the positive terminal of a power supply using alligator clips.

5 Immerse a platinum strip connected to the negative terminal of the same power supply using alligator clips.

6 Shine light on the sample to generate sufficient carriers for nano–porous etching to take place. Etching times may vary from 1 minute to 10 minutes.

The current flowing through the solution can be monitored using a known resistor and a standard voltmeter. This current must be adjusted using the voltage output on the power supply such that the pore formation condition as described in [26] is met. Figure 6–1 shows a schematic of this procedure.

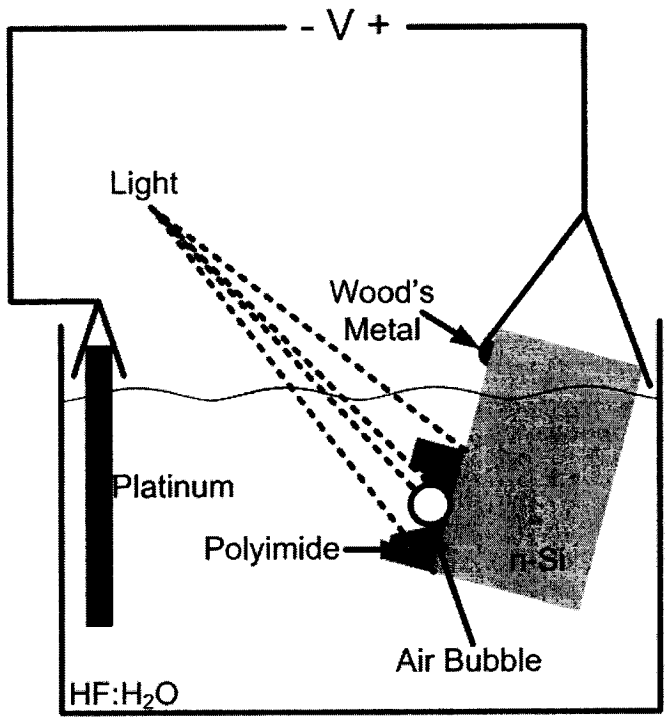

Figure 6–1: Schematic diagram showing fabrication of nano–porous silicon on an n–type silicon substrate.

It has been found that this procedure produces irregular and unpredictable nano–porous patterns on the n–type silicon surface. Upon close examination of the surface during the etching process, it is found that air bubbles can form at the silicon surface and become held there by the polyimide walls as shown in figure 6–1. The bubble prevents the solution from touching the silicon surface directly, thus reducing

the etching rate. These effects can be minimized if the diluting agent used is ethanol instead of water. In this case, the bubbles are much smaller and tend to float up and away from the silicon surface rapidly after forming. The ratio of ethanol to hydrofluoric acid used is 3 : 1.

Using the method of applying PEDOT:PSS described in chapter 4 to the nano–porous silicon surface is found to work poorly. The photovoltaic performance of the hybrid heterojunction with a nano–porous silicon layer is found to be inferior to the planar heterojunction described in this present work. It is hypothesized that this is due to the nano–pores not being completely filled by the PEDOT:PSS as shown in figure 6–2.

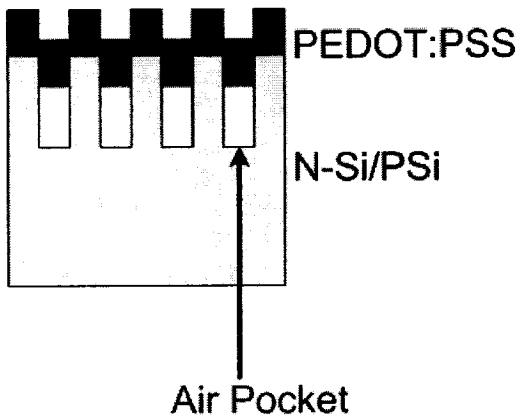

Figure 6–2: Diagram showing air pockets formed when PEDOT:PSS is spun onto nano–porous silicon.

The problem depicted in figure 6–2 is attempted to be eliminated by placing the sample into a vacuum chamber for 10 minutes after applying and spin coating the PEDOT:PSS but before baking in the oven. The hope is that the vacuum will suck the air out of the air pockets, forcing the PEDOT:PSS to completely fill the

nano–pore. This is found to improve performance significantly, although the current produced by illumination at low bias is reduced significantly as in sample 9.

The final work done on the nano–porous silicon sample involves placing the sample in a BHF solution in an attempt to remove surface states and thus enhance the current at low biases. Unfortunately, it is found that the BHF is so aggressive with the nano–porous silicon surface that it etches away not only any surface barrier layer, but also the nano–pores themselves.

CHAPTER 7
Conclusions & Future Work

7.1 Conclusions

With the cost of inorganic electronics being prohibitive and the performance of organic electronics being disappointing, it is natural to attempt to combine the two in the hopes that the positive elements of each can be exploited. These are known as hybrid devices. In the present work, the hybrid device consisting of an inorganic n–type silicon is matched with an organic polymer p–type PEDOT:PSS to form a hybrid heterojunction.

The primary function of the heterojunction is to absorb light, separate the exciton charges and transport the charges to the contacts. In the n-Si/PEDOT:PSS junction discussed in the present work, the bulk of the light absorption occurs in the n–type silicon while the PEDOT:PSS functions mainly to form the electric field to aid in the separation of charges and to provide a relatively low resistance medium to transport the charges.

Previous works have used inorganic substrates paired with organic (both small molecule and polymer) layers to form hybrid heterojunctions. Varying degrees of success have been reported with efficiencies ranging from 0.28% [12] to 17.5% [15]. Substrates have included n–type silicon, p–type silicon, various tin oxides, copper indium selenide and n–type gallium arsenide. The organic materials reported are too extensive to list here, but can be found in Appendix B.

The results of this present work are found to compare favourably with those listed in the literature review for n–type silicon substrates. Efficiencies as high as 0.63% are reported. Fill factors as high as 57% are reported. These are an improvement over other n-Si–based devices with the exception of devices consisting of a layered n–type silicon/nano–porous silicon/organic hybrid device (i.e. n-Si/PSi/organic). These three layered hybrid devices provide enhanced light absorption due to the different bandgap of nano–porous silicon from monocrystalline silicon, thus resulting in a higher efficiency than the device reported in the present work.

The objectives listed in the introduction of the present work have been achieved and the following can be concluded:

1 Device theory can be applied to justify the proposed structure in order to efficiently convert light into electricity.

2 Using modern and conventional electronic microfabrication techniques involving equipment no more complex than a spin coater, an oven and a vacuum deposition chamber, it is possible to fabricate the proposed structure.

3 The proposed structure converts light into electricity more efficiently than other devices of similar structures (i.e. hybrid heterojunctions using n–type silicon substrates) and of the same magnitude as other hybrid heterojunctions not using n–type silicon substrates.

7.2 Future Work

The first experiments that should be undertaken to add to the value of this present work is to simply analyze a different aspect of the same hybrid heterojunction. The device lifetime can be easily determined by selecting a sample and measuring its

I–V characteristics from the day it is fabricated to several weeks or months later, until its performance degrades beyond a specified threshold. The degradation threshold can be related to any of the figures of merit.

Along the same lines, devising a method of encapsulation and packaging in order to prolong the usable lifetime of these hybrid heterojunctions would provide very useful not only for long-term characterization, but also for industrial scale production.

Considering the observations from existing work carried out (as described in the Additional Work chapter), the recommendation for future work in this field involves perfecting a method for producing a nano–porous silicon surface that is devoid of any barrier layer. This could either be done by finding an etchant that will remove any impurities and oxides from the nano–porous silicon surface without attacking the nano–porous silicon itself, or by simultaneously removing an oxide or impurity layer and forming the nano–pores in the silicon surface.

Developing such a method, in combination with a confirmed method for filling PEDOT:PSS into the nano–porous silicon should yield improved photovoltaic efficiency, η.

Appendix A: List of Symbols

Symbol	Definition
R_S	series resistance
I_{SC}	short circuit current
J_{SC}	short circuit current density
V_{OC}	open circuit voltage
MPP	maximum power point
FF	fill factor
η	power conversion efficiency

Appendix B: List of Chemical Abbreviations

Abbreviation	Chemical Composition
	ORGANIC
α-NPD	N,N'-(α-naphthyl)-N,N'-diphenyl-1,1'-biphenyl-4,4'-diamine
CuPC	copper phthalocyanine
MEH-PPV	poly(2-methoxy-5-(2'-ethyl-hexyloxy)-1,4-phenylene vinylene)
P3OT	poly(3-octylthiophene)
p-TPA	poly(N,N'-diphenyl-4-styrene)
PA-PPV	phenylamino-p-phenylenevinylene
PAn	polyaniline
PBD	2-(biphenyl-4-yl)-5-(4-tert-butylphenyl)-(1,3,4-oxadiazole)
PEDOT	poly(3,4-ethylenedioxythiophene)
PMeT	poly(3-methylthiophene)
poly(ET2)	poly(4,4'-dipentoxy-2,2'-bithiophene)
PP-Th	polythiophene
PPy	polypyrrole
PSS	poly(styrenesulfonate)
TCQ	tetrachloroquinone
TPA	triphenylamine
TPD	N,N'-diphenyl-(1,1'-biphenyl)4,4'-diamine
	INORGANIC
BHF	buffered hydroflouric acid solution
CIS	copper indium selenide
i-ZnO	intrinsic zinc oxide
ITO	indium tin oxide
n-GaAs	n-type gallium arsenide
n-Si	n-type silicon
n-ZnO	n-type zinc oxide
p-Si	p-type silicon
PSi	nano-porous silicon

References

[1] S. Smith and S. R. Forrest, "A low switching voltage organic-on-inorganic heterojunction memory element utilizing a conductive polymer fuse on a doped silicon substrate," *Applied Physics Letters*, vol. 84, no. 24, pp. 5019–5021, 2004.

[2] M. Schubert, C. Bundesmann, H. v. Wenckstern, G. Jakopic, A. Haase, N.-K. Persson, F. Zhang, H. Arwin, and O. Inganas, "Carrier redistribution in organic/inorganic (poly(3,4-ethylenedioxythiophene)/poly(styrenesulfonate)polymer-si) heterojunction determined from infrared ellipsometry," *Applied Physics Letters*, vol. 84, no. 8, pp. 1311–1313, 2004.

[3] A. Ltaief, J. Davenas, A. Bouazizi, R. Ben Chaâbane, P. Alcouffe, and H. Ben Ouada, "Film morphology effects on the electrical and optical properties of bulk heterojunction organic solar cells based on MEH-PPV/C_{60} composite," *Materials Science and Engineering C*, vol. 25, no. 1, pp. 67–75, 2005.

[4] A. Ltaief, A. Bouazizi, J. Davenas, R. Ben Chaâbane, and H. Ben Ouada, "Electrical and optical properties of thin films based on MEH-PPV/fullerene blends," *Synthetic Metals*, vol. 147, no. 1–3, pp. 261–266, 2004.

[5] D. H. Shin, S. D. Lee, K. P. Lee, S. Y. Park, D. H. Choi, and N. Kim, "Characteristics of heterojunction consisting of plasma polymerized thiophene and n-type silicon," *Synthetic Metals*, vol. 71, no. 1–3, pp. 2263–2264, 1995.

[6] N. Camaioni, G. Beggiato, G. Casalbore-Miceli, M. C. Gallazzi, A. Geri, and A. Martelli, "Photovoltaic effect of heterojunctions between poly(4,4-dipentoxy-2,2'-bithiophene) and n-doped silicon," *Synthetic Metals*, vol. 85, no. 1–3, pp. 1369–1370, 1997.

[7] N. Camaioni, G. Beggiato, G. Casalbore-Miceli, A. Geri, A. Martelli, and L. Ventura, "Photovoltaic and transport properties of the heterojunction between poly(4,4-dipentoxy-2,2bithiophene) and n-doped silicon," *Solar Energy Materials and Solar Cells*, vol. 53, no. 3–4, pp. 217–227, 1998.

[8] R. Yuan, H. Yuan, Z. Zou, Y. Zheng, and Y. Wang, "Polyaniline/silicon heterojunctions," *Synthetic Metals*, vol. 41, no. 1–2, pp. 731–734, 1991.

[9] J. M. G. Laranjeira, H. J. Khoury, W. M. d. Azevado, E. F. d. J. Silva, and E. A. d. Vasconcelos, "Fabrication of high quality silicon–polyaniline heterojunctions," *Applied Surface Science*, vol. 190, no. 1–4, pp. 390–394, 2002.

[10] I. Musa and W. Eccleston, "Electrical properties of polymer/si heterojunctions," *Thin Solid Films*, vol. 343–344, pp. 469–475, 1999.

[11] Z. H. Yang, P. Zhang, D. J. Wang, D. Zhang, X. D. Chai, and T. J. Li, "Optoelectronic behaviour of conjugated polymer/silicon heterojunctions," *Synthetic Metals*, vol. 85, no. 1–3, pp. 1293–1294, 1997.

[12] M. Y. Song, K.-J. Kim, and D. Y. Kim, "Enhancement of photovoltaic characteristics using a PEDOT interlayer in TiO_2/MEHPPV heterojunction devices," *Solar Energy Materials & Solar Cells*, vol. 85, no. 1, pp. 31–39, 2005.

[13] A. C. Arango, L. R. Johnson, V. N. Bliznyuk, Z. Schlesinger, S. A. Carter, and H.-H. Hoerhold, "Efficient titanium oxide/conjugated polymer photovoltaics for solar energy conversion," *Advanced Materials*, vol. 12, no. 22, pp. 1689–1692, 2000.

[14] S. Bereznev, I. Konovalov, A. Opik, and J. Kois, "Hybrid $CuInS_2$/polypyrrole and $CuInS_2$/poly(3,4-ethylenedioxythiophene) photovoltaic structures," *Synthetic Metals*, vol. 152, no. 1–3, pp. 81–84, 2005.

[15] F. Garnier, "Hybrid organic-on-inorganic photovoltaic devices," *Journal of Optics A: Pure and Applied Optics*, vol. 4, no. 6, pp. S247–S251, 2002.

[16] C. H. Yang, Q. Qiao, J. Sun, K. J. Jiang, Y. L. Li, and Y. F. Li, "Improvement of the performance of polymer/C_{60} photovoltaic cells by small-molecule doping," *Synthetic Metals*, vol. 137, no. 1–3, pp. 1521–1522, 2003.

[17] N. Tokranova, I. Levitsky, B. Xu, J. Castracane, and W. Euler, "Hybrid solar cells based on organic material embedded into porous silicon," in *Proceedings of SPIE: Organic Photonic Materials and Devices VII*, vol. 5724, (San Jose, CA, USA), pp. 183–190, 2005.

[18] G. P. Kushto, W. Kim, and Z. H. Kafafi, "Flexible organic photovoltaics using conducting polymer electrodes," *Applied Physics Letters*, vol. 86, no. 9, p. 093502, 2005.

[19] H. Hovel, *Semiconductors and Semimetals, Volume 11.* Academic Press, 1976.

[20] C. Brabec, V. Dyakonov, J. Parisi, and N. S. Sariciftci, *Organic Photovoltaics:Concepts and Realization.* Springer, 2003.

[21] F. C. Krebs, J. E. Carlé, N. Cruys-Bagger, M. Andersen, M. R. Lilliedal, M. A. Hammond, and S. Hvidt, "Lifetimes of organic photovoltaics: photochemistry, atmosphere effects and barrier layers in ITO-MEHPPV:PCBM-aluminium devices," *Solar Energy Materials & Solar Cells*, vol. 86, no. 4, pp. 499–516, 2005.

[22] Sigma-Aldrich, *483095 Poly 3 4-ethylenedioxythiophene poly styrenesulfonate 1.3 wt % dispersion in H_2O, conductive grade*, 2006.

[23] OBB, *Light Sources: Lamp Emission Spectra*, 2004.

[24] D. A. Neamen, *Semiconductor Physics and Devices, Basic Principles: Second Edition.* Irwin, 1997.

[25] M. Madou, *Fundamentals of Microfabrication.* CRC Press, 1997.

[26] P. C. Searson and J. M. Macaulay, "Fabrication of porous silicon structures," *Nanotechnology*, vol. 3, no. 4, pp. 188–191, 1992.